PRESSURE-DRIVEN FLOW OF A SUSPENSION: BUOYANCY EFFECTS

J. F. MORRIS† and J. F. BRADY

Division of Chemistry and Chemical Engineering, California Institute of Technology, Pasadena, CA 91125, U.S.A.

Abstract—Dynamic simulation of pressure-driven flow of a non-neutrally buoyant suspension has been performed by Stokesian Dynamics. Channel flow at zero Reynolds number of a monodisperse non-Brownian suspension of spheres in a monolayer was studied for a range of three parameters: bulk particle area fraction ϕ_A^b, dimensionless gravitational parameter $B = (U^0/\langle u \rangle)(H/a)^2$, and dimensionless channel width H/a. Here, U^0 is the Stokes settling velocity of an isolated sphere, $\langle u \rangle$ is the mean velocity of the suspension, H is the channel width, and a is the particle radius. From an initially uniform distribution, a range of behavior in the fully-developed flow is observed depending upon the value of B. For small B, shear-induced migration dominates buoyancy effects, and a layer at large ϕ_A is formed in the center of the channel. For sufficiently strong gravitation, particles settle rapidly to form a concentrated layer that is transported along the bottom of the channel by shearing. At intermediate values of B, shear-induced migration of particles to the center of the channel occurs simultaneously with gravitational settling. In the lower portion of the channel, these fluxes are opposed and lead to nonmonotonic variation of particle fraction, with ϕ_A increasing away from the lower wall to a maximum near or even above the centerline and then rapidly decreasing, typically vanishing to leave clear fluid adjacent to the upper wall. These results are in qualitative agreement with the small amount of experimental data in the literature on such systems. The flow has been modeled using macroscopic balance equations presented previously; the predictions agree well with simulations. © 1997 Elsevier Science Ltd

Key Words: suspensions, pressure-driven flow, buoyancy, shear-induced migration, flow modeling, non-Newtonian rheology

1. INTRODUCTION

Suspensions exhibit a variety of rheological responses. The dependence of the viscosity upon the particle volume fraction ϕ is strong, and even suspensions with weak interparticle forces and weak Brownian motion exhibit non-Newtonian behavior, including normal stress differences (Gadala-Maria 1979, Brady & Morris 1997) and time-dependent rheology (Gadala-Maria & Acrivos 1980). These rheological phenomena in uniformly concentrated and homogeneously sheared suspensions are compounded in inhomogeneously sheared suspensions by shear-induced particle migration (Leighton & Acrivos 1987b). This irreversible migration of noncolloidal particles can result in very nonuniform concentration fields, and the pervasiveness of flows with varying shear rate—that is flows in which the shear rate or stress vary with position as in pipe flow for example—makes understanding particle migration important for process design. If particles and fluid are not of the same density, settling (or rising) occurs simultaneously with shear-induced migration, and the bulk flow also depends upon the relative strength of buoyancy and shearing forces.

This work investigates the influence of particle buoyancy in inhomogeneous suspension flow. Inhomogeneous here means the shear rate is nonconstant, whereas we reserve the term nonuniform for variation in particle fraction. We have studied pressure-driven flow of a suspension of heavy particles in a channel (there is no loss of generality in assuming the particles more dense than the fluid). The flow was simulated by Stokesian Dynamics over a range of the relevant dimensionless parameters, which are the bulk particle area fraction ϕ_A^b (area rather than volume fraction because

---

†Present address: School of Chemical Engineering, Georgia Institute of Technology, Atlanta, GA 30332, U.S.A.

we simulate flow in a monolayer), the ratio of channel width to particle size H/a, and $B = (U^0/\langle u \rangle)(H/a)^2$, where U^0 is the Stokes settling velocity of an isolated particle and $\langle u \rangle$ is the average velocity of the suspension; B characterizes the relative strength of buoyancy to viscous shearing. We have also extended the application of the suspension-flow model presented by Nott and Brady (1994), hereafter referred to as NB, to non-neutrally-buoyant particle flows. The model equations were solved to predict the fully-developed flow over a range of parameters. The agreement between the simulation results and model predictions is good over a wide range of B.

There is little experimental work that is directly comparable with our simulations of channel flow. While there is no replacement for physical experiments, confidence that the simulation results represent realistic behavior is well-founded: Stokesian Dynamics simulations of Phung et al. (1996) and Phung (1993) yield excellent agreement with the suspension viscosity determined experimentally by van der Werff and de Kruif (1989) and with the particle microstructure determined in experiments by Parsi and Gadala-Maria (1987). For pressure-driven flow, there is good agreement between the simulations of NB and the experiments of Koh et al. (1994).

An interesting density stratification in which relatively heavy material flows stably above lighter results from competition between buoyancy forces and shear-induced migration. This was observed by Altobelli et al. (1991), who performed nuclear magnetic resonance (NMR) imaging of the velocity and particle fraction in pressure-driven tube flow (note their figure 6). Shear-induced migration gives rise to a maximum in ϕ near the center of the tube, similar to the findings of Koh et al. (1994). The results of Altobelli et al. are particularly interesting, however, because the particle density exceeds the fluid density, and thus the suspension of large ϕ near the center of the tube is denser than the more dilute suspension below. Zhang and Acrivos (1994) have modeled the flow in the experiments of Altobelli et al., showing that the volume-fraction profiles can be explained by a balance of shear-induced migration and gravitational settling; their model also predicts a nonaxial mean secondary flow. Our simulations demonstrate that a similar density stratification occurs in two-dimensional channel flow over a range of ϕ_A^b and B.

Indeed, a density stratification with heavy material over light is to be expected in pressure-driven flow. In a neutrally-buoyant suspension, particles migrate to the center of the channel where the shear rate is small. Thus, if the mass density of the particles increases by a small amount, the concentration profile will be slightly perturbed and the concentrated suspension at the center of the channel will be denser than the dilute material below. Were this not the case, the condition of neutral buoyancy would be unstable and probably unobservable.

Pressure-driven flow with heavy particles involves the phenomenon of viscous resuspension. In resuspension, a settled layer of heavy particles expands in height and flows due to shear in the fluid above. Resuspensions at large Reynolds numbers, such as those involved in transport of sand and silt in surf zones, are well-known. In contrast to these inertially-dominated phenomena, viscous resuspension occurs at small Reynolds number where inertia has negligible influence. Leighton and Acrivos (1986) showed that the steady-state height of a viscously-suspended layer could be estimated from a balance between gravitational settling and Fickian diffusion of particles. The particles were assumed to be too large for Brownian diffusion to play a significant role; hence, the diffusivity in this model is the shear-induced diffusivity driven by hydrodynamic interactions. This gradient- or collective-diffusivity is to be distinguished from the closely related shear-induced self-diffusivity first recognized and studied by Eckstein et al. (1977).

Leighton and Acrivos (1987a, b) improved upon the experimental technique of Eckstein et al. (1977), and made the important step of relating the cross-stream migration of particle to fluxes caused by gradients in both shear rate $\dot{\gamma}$ and concentration ϕ. This "diffusive flux" phenomenology has been used in a number of suspension-flow models. Schaflinger et al. (1990) applied it in modeling a suspension of dense particles in shear and pressure-driven channel flow, but included only the particle flux due to $\nabla \phi$. For pressure-driven channel flow of heavy particles, the model predicts that all particles lie below the velocity maximum. This prediction, which is contradicted by the simulation results of the present study, is readily understood because the cross-stream flux at the maximum in axial velocity (i.e. where $\dot{\gamma} = 0$) is solely due to gravitational settling, and the particles must lie below the velocity maximum. Phillips et al. (1992) included the particle flux due to both $\nabla \dot{\gamma}$ and $\nabla \phi$, successfully predicting rates of variation and steady-state values for ϕ in inhomogeneous shear flows of neutrally-buoyant suspensions. However, there was again

discrepancy from experimental results for pressure-driven flow, as the model predicted, for all bulk particle fractions, that ϕ would take on the maximum value $\phi = \phi_m$ at the location where the velocity gradient vanishes. Zhang and Acrivos (1994) applied the diffusive-flux model with migration due to both $\nabla\phi$ and $\nabla\dot{\gamma}$ to predict pressure-driven tube flow of a suspension of heavy particles, and their predictions are in good agreement with the experiments of Altobelli $et\ al.$ (1991).

The suspension-balance model of NB is used in the present study. The suspension-balance approach differs from the diffusive-flux approach in two notable and closely related ways. The first is in the rheological model for the suspension and the second is in the manner in which particle migration is incorporated. The diffusive flux model employs a Newtonian rheology with a ϕ-dependent shear viscosity and postulates a form for the cross-stream flux. The suspension-balance model employs a non-Newtonian bulk stress with shear-induced normal stresses and relates the cross-stream flux of particles to the variation of the normal stresses. In this and prior applications of the suspension-balance model, only the isotropic normal stress, or particle pressure Π (Jeffrey $et\ al.$ 1993) was used, because normal stress differences are not relevant to the rectilinear flows considered. However, NB did note that normal stress differences should be included in the general case, and their origin and importance have been demonstrated by Brady and Morris (1997).

The prediction by the diffusive-flux model of a particle fraction maximum of $\phi = \phi_m$ at the centerline in pressure-driven flow prompted NB to model the particle pressure Π nonlocally. Rather than a pressure proportional to $\dot{\gamma}$ as dimensional considerations suggest, NB, following arguments presented by Jenkins and McTigue (1990) for the influence of fluctuational motion in suspensions, modeled Π proportional to $\sqrt{T}$, where $T = \langle u' \cdot u' \rangle_p$ (defined pointwise) is the mean square of the scalar particle velocity fluctuations†. A balance equation for T including diffusive transport of fluctuational "energy" was postulated using heuristic arguments based upon the equation for the rate of dissipation of energy in the suspension. Expressing $\Pi \propto \sqrt{T}$ is a simple means of constructing a nonlocal model for the suspension stress. The model asserts that T is generated at points where $\dot{\gamma}$ is large and is transported diffusively if not spatially constant, and the constitutive relation of Π to $\sqrt{T}$ renders the stress nonlocal in $\dot{\gamma}$. An alternative nonlocal approach to modeling the bulk shear stress in pressure-driven flow has been proposed by Mills and Snabre (1996) and used with good success in predicting the pressure driven channel flows of Koh $et\ al.$ (1994).

We have simulated the pressure-driven flow of a suspension over a range of B to assess the dependence of the flow behavior upon the relative strength of settling to migration. A wide range of behavior is observed, from the neutrally-buoyant suspension $(B = 0)$, in which a highly-concentrated layer of particles forms at the center of the channel, to the formation of a settled layer of particles which are transported along the bottom of the channel by shear for sufficiently large B. At small and intermediate B, a stable flow of heavy material over light occurs. The bulk flow depends strongly upon ϕ_A^b: for small ϕ_A^b at a fixed B, buoyancy is more important relative to shear-induced migration than at larger concentrations. Fixing B and ϕ_A^b effectively yields dynamic similarity, and the residual influence of H/a is weak, with the primary effect being that T is larger in the center of the channel for narrower channels. All of the simulations reported employed a short-ranged repulsive interparticle force. These forces apparently have an important influence upon the bulk flow behavior, as shown by Brady and Morris (1997) and discussed in section 2.2.

In this work, we have not studied highly-concentrated suspensions The equivalent volume fractions of the monolayer simulations reported are roughly $0.27 \leqslant \phi \leqslant 0.4$. Our interest in this work was to understand the migration phenomenon in situations where particle buoyancy is relevant and to determine the validity of the suspension-balance flow model in these situations. In a suspension where ϕ is close to the maximum packing value ϕ_m, little migration will be observed, as any migration forces some region of the flow to reach $\phi = \phi_m$. Hence, for purposes of a study of migration, the moderately concentrated suspensions are of greater interest, as variation of the particle fraction across the flow can be on the order of 100% rather than only a few per cent.

We begin in section 2 by discussing the development length of the flow, the buoyancy parameter,

---

†There is no potential for confusion of the meaning of the symbol T here, as the particles are assumed non-Brownian and the thermodynamic temperature is never considered.

and the influence of interparticle forces. In section 3, application of Stokesian Dynamics to this flow is discussed and the simulation results are presented. Predictions of the flow by the model are compared with simulation results in section 4, followed by a summary and discussion.

2. SCALING ANALYSIS AND THE ROLE OF INTERPARTICLE FORCES

2.1. *Flow development and the buoyancy parameter*

We consider pressure-driven flow of a non-Brownian suspension of spheres in a Newtonian fluid at vanishing Reynolds number. The particles are of equal or greater density than the fluid and interact both hydrodynamically and through repulsive interparticle forces, the latter vanishing at surface separations much smaller than the particle size. The inhomogeneous shear rate in pressure-driven flow causes particle migration to the center of the channel, and heavy particles settle due to gravity. For a suspension of initially uniform particle fraction flowing in an arbitrarily long channel (the situation in our simulations), there is no variation in the streamwise direction. The concentration profile evolves in time in a manner that depends on the relative strength of shear-driven to buoyancy-driven fluxes.

For a neutrally buoyant noncolloidal suspension, an estimate of the length scale for evolution of ϕ, obtained by NB using an argument due to Leighton and Acrivos (1987b), shows that fully-developed pressure-driven channel flow should be expected after a distance of $O[(H/a)^2H]$. The argument is that particles migrate a distance of $O(H)$ by a random-walk process characterized by the shear-induced self-diffusivity (Eckstein *et al.* 1977). This diffusivity scales, on dimensional grounds, as $\dot{\gamma}a^2\mathscr{D}(\phi)$, where $\mathscr{D}$ is a dimensionless function of particle concentration. Diffusive motion of lengthscale H occurs in a time $H^2/(\dot{\gamma}a^2\mathscr{D})$, while $\dot{\gamma}H$ is a representative velocity scale, and the product of these time and velocity scales yields the flow rate-independent $(H/a)^2H/\mathscr{D}$ as an estimate of the development length. For $\phi > 0.3$, $\mathscr{D} \approx 0.1$ from the experiments of Leighton and Acrivos (1987a) and Stokesian Dynamics simulations of Phung (1993). When particle buoyancy is relevant, this estimate serves as an upper limit; development is understandably more rapid for very dense particles as settling dominates migration.

We define a dimensionless parameter B characterizing the relative strength of buoyancy to shearing. A shear-driven random walk of $O(H)$ takes a time of $O(H^2/\dot{\gamma}a^2) = O(H^3/\langle u\rangle a^2)$, with $\dot{\gamma} = \langle u\rangle/H$, while Stokes settling velocity yields an estimate of H/U^0 for the time to settle a similar distance, and the ratio of these two times is

$$B \equiv \left(\frac{U^0}{\langle u\rangle}\right)\left(\frac{H}{a}\right)^2. \tag{1}$$

The Stokes settling velocity is $U^0 = 2(\rho_p - \rho_f)ga^2/9\eta$, with $g = |\mathbf{g}|$ the magnitude of the gravitational acceleration, so that B may also be written

$$B = \frac{2(\rho_p - \rho_f)gH^2}{9\eta\langle u\rangle} = O\left(\frac{(\rho_p - \rho_f)g}{|\nabla P|}\right),$$

where ∇P is the pressure gradient driving the flow. Note that B is inversely proportional to the Shields parameter κ used by Schaflinger *et al.* (1990).

The parameters B, bulk particle fraction ϕ^b, and dimensionless channel width H/a characterize the channel flow of a suspension. A simple rescaling of the particle fraction discussed in section 4 allows constitutive relations developed for three-dimensional systems to be applied to a monolayer.

2.2. *Repulsive interparticle forces*

Interparticle forces were neglected in the above scaling analysis, although there generally should be further dimensionless groups characterizing the strength and range of these forces relative to the shear flow and particle size. Throughout our simulations we maintain the same ratio of shear

rate to strength of interparticle force and the same range of interparticle force, so their variation is not an issue in the simulations.

We have found, similar to NB, that repulsive interparticle forces do, however, have important consequences for the flow. Short-ranged repulsive forces, i.e. forces vanishing at interparticle separations much smaller than the particle radius, which are the type of forces used here, inhibit the formation of closely packed particle clusters. This was observed in the simulation of NB and also in undisplayed work from this study. Particle clusters can often span a large fraction of the channel, and the flow is consequently not representative of a smoothly-sheared suspension. In essence, H/l is not large, where l is a measure of the cluster size, and thus "wall" effects dominate the suspension motion. In order to obtain a clear picture of the migration phenomenon and simulation results that could be compared with a flow model that assumes smooth shearing, repulsive interparticle forces were used in all of the simulations reported.

Recent analysis of the pair distribution function for suspensions of monodisperse spheres in strong flow—i.e. flow at large Péclet number Pe where the Péclet number measures the relative strength of shearing to Brownian motion—has shown that if a repulsive force or surface roughness is present, the rheology of a dilute suspension is non-Newtonian with finite particle pressure and normal stress differences in the limit Pe $\rightarrow \infty$ (Brady & Morris 1997). Hence, the introduction of a repulsive force is sufficient to produce the non-Newtonian behavior assumed in the model detailed in section 4. Extensions of these results to concentrated suspensions using arguments for the interaction of a close pair in the "mean field" of a concentrated suspension were presented in Brady and Morris (1997), and it was shown that the shear and normal stresses in strongly-sheared concentrated suspensions are of comparable magnitude and scale in the same manner as maximum packing is approached. Large scale particle clustering was not addressed in this study. In concentrated colloidal suspensions ($\phi > 0.5$), transient clusters have been shown to be closely correlated with shear thickening at large shear rates (Bossis & Brady 1989, D'Haene et al. 1993, Bender & Wagner 1996). Thus, if strong particle clustering occurs, the "microscale" length scale will increase from the particle size a to the cluster size l, and the macroscopic modeling would need to explicitly take into account this new length scale.

3. SIMULATION

Stokesian Dynamics simulations of pressure-driven channel flow were performed for a range of ϕ_A^b and B, at two values of H/a. Complete descriptions of Stokesian Dynamics are given elsewhere (Brady et al. 1988, Brady & Bossis 1988), while application of the method to pressure-driven flow was demonstrated by NB. We present only a brief treatment of the method before turning to the simulation results.

3.1. Simulation method

The Stokesian Dynamics method for simulation of suspension flow captures both the near-field and the many-body nature of hydrodynamic interactions at low Reynolds number. This is possible because hydrodynamic interactions may be decomposed into short-ranged lubrication interactions and long-ranged mobility interactions. Mobility interactions are computed as an expansion in moments about the particle centers of the hydrodynamic force density exerted on the particle surfaces. In application, the expansion is truncated after the first moment, where the zeroth moment is the net force on a particle, and the first moment consists of the antisymmetric torque and the symmetric stresslet. Faxén's laws (Kim & Karrila 1991) for the motion of a particle in given velocity fields are used along with the moment expansion to construct the grand mobility tensor $\mathcal{M}^\infty$. To simulate a medium of infinite extent, a unit cell containing a finite number of particles is periodically replicated throughout space. Interactions between all particles are summed, with Ewald's summation technique (Beenakker 1986) used to speed convergence. The grand mobility tensor is inverted to give a far-field approximation, $\mathcal{R}^\infty = (\mathcal{M}^\infty)^{-1}$, of the grand resistance tensor $\mathcal{R}$. It is in this inversion that many-body interactions are incorporated: while the construction of $\mathcal{M}^\infty$ was performed pairwise, the inversion sums the series of reflected interactions among all particles. Near-field lubrication interactions, which are two-body interactions even in a concentrated
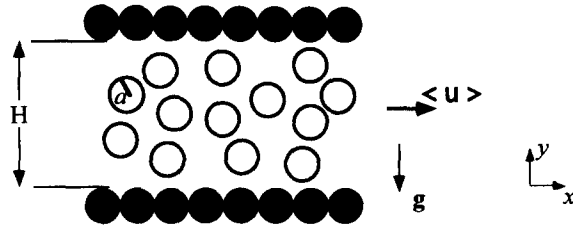
Figure 1. Schematic representation of the unit cell employed in the simulation of a pressure-driven channel flow of non-neutrally buoyant particles. The shaded wall particles are fixed while the unshaded interior particles are free to move in the x–y plane. Gravity acts in the negative y-direction. Only the particles of one wall are within the unit cell; the second wall is included for appearance.

suspension, are added to the grand resistance tensor in pairwise fashion, with the portion of the near-field interaction captured by the far-field approximation subtracted to avoid double-counting, thus yielding the grand resistance tensor $\mathscr{R}$. Note that $\mathscr{R}$ is a function only of the particle configuration.

The hydrodynamic forces, torques, and stresslets on the N particles in the unit cell are related through $\mathscr{R}$ to the particle velocities and the average rate of strain by

$$\begin{pmatrix} \mathbf{F} \\ \mathbf{S} \end{pmatrix} = -\mathscr{R} \cdot \begin{pmatrix} \mathbf{u} - \langle \mathbf{u} \rangle \\ -\langle \mathbf{e} \rangle \end{pmatrix}, \qquad [2]$$

where

$$\mathscr{R} = \begin{bmatrix} \mathbf{R}_{FU} & \mathbf{R}_{FE} \\ \mathbf{R}_{SU} & \mathbf{R}_{SE} \end{bmatrix}. \qquad [3]$$

In [2], $\mathbf{u}$ is the $6N$ vector of particle velocities (translational and rotational); $\langle \mathbf{u} \rangle$ and $\langle \mathbf{e} \rangle$ are the average velocity and the average rate of strain, respectively, of the bulk suspension; $\mathbf{F}$ is the vector of hydrodynamic forces and torques; and $\mathbf{S}$ is the N-particle stresslet exerted by the fluid on the particles. Couplings in [3] are indicated by subscripts: $\mathbf{R}_{FU}$ is the resistance tensor coupling force/torque to velocity/angular velocity, $\mathbf{R}_{SE}$ couples stresslet to rate of strain, and the others are clear from these.

Simulation of pressure-driven flow requires simulating a boundary, which may be accomplished either through a numerical approximation of a wall as discretized flat patches (Durlofsky & Brady 1989) or by allowing a group of the particles to mimic a wall by moving together at a fixed velocity. We use the latter method. This method, which NB have shown captures the essential physical features of the flow, is simpler because the hydrodynamic interaction between a "wall" particle and a suspended "interior" particle is no different from that between two suspended particles, whereas in the flat-wall approach the interaction of a sphere with the wall must be separately approximated. The N particles in the unit cell are divided into the N_w that make up the wall, and the remaining $N_i = N - N_w$ suspended particles. The unit cell is schematically illustrated (along with the wall particles of a neighboring image cell) in figure 1. Note that we simulate a monolayer in order to save computational expense.

The wall particles are constrained to move at a prescribed velocity, while the interior particles move freely in the x- and y-directions (we simulate a monolayer in the (x, y) plane) in such a way that the net force (hydrodynamic plus nonhydrodynamic) on each is zero in accordance with inertialess flow. The forces on the wall particles and the velocities of the interior particles are to be determined. The overall strain rate $\langle \mathbf{e} \rangle$ is zero† and the average suspension velocity $\langle \mathbf{u} \rangle$ is prescribed. A pressure gradient is established to drive the flow, and this pressure gradient balances the force necessary to maintain the wall particle velocities, thus satisfying the requirement that the net force upon the unit cell vanishes. Buoyancy is incorporated by exerting a constant force $\mathbf{F}_g$ upon

---

†This $\langle \mathbf{e} \rangle$ is the cell-averaged rate of strain required in the Stokesian Dynamics method. A local average of the rate of strain in the flow is nonzero in general, although it does vanish at some plane in pressure-driven flow.

each interior particle. As discussed in section 2.2, pairwise interparticle forces are simulated, with the force on particle α due to particle β given by

$$\mathbf{F}_{\alpha\beta}^{IP} = F_0 \frac{\tau \exp[-\tau\varepsilon]}{1 - \exp[-\tau\epsilon]} \mathbf{d}_{\alpha\beta},$$ [4]

where $\epsilon = r/a - 2$ is the dimensionless distance between the sphere surfaces, and $\mathbf{d}_{\alpha\beta}$ is the unit vector directed from sphere α to sphere β. The parameter τ determines the range of the force, while the product $F_0\tau$ fixes the strength. For $\tau = 1000$ as used in the reported simulations, the force scaled by $6\pi\eta a\langle u\rangle$ is unity at a surface separation of about $5 \times 10^{-5}a$.

Fixing the wall velocity at zero, the equation of motion for the particles is

$$\begin{pmatrix} \mathbf{F}^w \\ \mathbf{F}^i \end{pmatrix} = \begin{pmatrix} \mathbf{F}^w \\ 0 \end{pmatrix} = -\begin{bmatrix} \mathbf{R}_{FU}^{ww} & \mathbf{R}_{FU}^{wi} \\ \mathbf{R}_{FU}^{iw} & \mathbf{R}_{FU}^{ii} \end{bmatrix} \cdot \begin{pmatrix} -\langle\mathbf{u}\rangle \\ \mathbf{u}^i - \langle\mathbf{u}\rangle \end{pmatrix} + \begin{pmatrix} \mathbf{F}_{IP}^w \\ \mathbf{F}_{IP}^i \end{pmatrix} + \begin{pmatrix} 0 \\ \mathbf{F}_g \end{pmatrix}.$$ [5]

We have decomposed $\mathbf{R}_{FU}$, denoting couplings by superscripts: $\mathbf{R}^{ww}$ is the resistance tensor denoting the interaction among wall particles, $\mathbf{R}^{wi}$ denotes the interaction of wall with interior particles, and so forth. Solving [5] for the suspended particle velocities yields

$$\frac{d\mathbf{x}^i}{dt} = \mathbf{u}^i = \langle\mathbf{u}\rangle + (\mathbf{R}_{FU}^{ii})^{-1}\cdot(\mathbf{R}_{FU}^{iw}\cdot\langle\mathbf{u}\rangle + \mathbf{F}_{IP}^i + \mathbf{F}_g)$$ [6]

where $\mathbf{x}^i$ is the N_i-particle position vector. Having constructed the resistance tensor, the positions are updated using [6] and the procedure is repeated. The near-field lubrication portion of the resistance tensor varies significantly for small relative motions of the particles, and is updated at each step in the evolution, whereas the far-field approximation obtained as the mobility invert $\mathscr{R}^\infty$ changes significantly only for relative motions of neighboring particles on the order of the particle size and is updated less frequently.

The set of ordinary differential equations [6] is completely coupled in the sense that a particle's motion depends upon the position of all other particles in the unit cell. Hydrodynamic interactions are nonlinear in particle position, and thus, as pointed out by NB, these equations exhibit deterministic chaos.

3.2. Results

We discuss nine simulations, with conditions and selected results summarized in table 1. The simulations are labeled in column 1. Input parameters are listed in columns 2–8: ϕ_A^b, H/a, and B are given in columns 2–4, respectively; the number of particles and the number making up the wall in the unit cell are listed in columns 5 and 6, respectively; column 7 lists $F_0\tau$, the interparticle force constant and column 8 lists the dimensionless computational time step Δt (time is scaled by $a/\langle u\rangle$). Taking $F_0\tau = 1.0$ and 0.6 for $H/a = 18.32$ and 30.54, respectively, the repulsive force has the same magnitude relative to the shear rate for all simulations, because $\langle u\rangle$ is fixed. The approximate dimensionless time t_{ss}, required to achieve a steady fully-developed flow is given in column 9. Columns 10 and 11 provide qualitative measures of the fully-developed flow behavior. In column

Table 1. Summary of the simulations discussed. Columns 2–8 list input parameters, column 9 lists the approximate times to achieve fully-developed flow, and columns 10 and 11 provide qualitative measures of the fully-developed bulk flow. Simulations G1 and G2 differ only in the separation between the monolayers: in G1 the layers are adjacent, while in G2 they are separated by four particle radii

Simulation	ϕ_A^b	H/a	B	N	N_w	$F_0\tau$	Δt	t_{ss}	$\bar{h}_x$	Q_p
A	0.4	30.54	0	79	9	0.6	0.05	12,000	0.49	1.20
B	0.4	30.54	3.4	79	9	0.6	0.05	4000	0.46	1.17
C	0.4	30.54	11.7	79	9	0.6	0.05	4000	0.40	1.14
D	0.4	30.54	16.8	79	9	0.6	0.05	3500	0.35	0.97
E	0.2	30.54	11.7	44	9	0.6	0.05	3200	0.21	0.62
F	0.6	30.54	11.7	114	9	0.6	0.05	4000	0.45	1.07
G1	0.4	18.32	3.4	51	9	1.0	0.05	1600	0.43	1.05
G2	0.4	18.32	3.4	51	9	1.0	0.05	2000	0.45	1.02
H	0.4	18.32	3.4	102	18	1.0	0.05	1800	0.46	1.14

10 is the average distance, scaled by H, of the suspended particles from the lower wall, denoted $\bar{h}_x$. Column 11 lists the particle flux normalized by its value for a uniformly dispersed suspension

$$Q_p = \frac{1}{\phi_A^b \langle u \rangle} \int_0^1 \phi_A(y) u(y) \, dy. \qquad [7]$$

We present profiles of ϕ_A, $\langle u \rangle$, and T averaged over 500 dimensionless time units, with averaging begun after the flow is fully-developed based on the criterion that $\bar{h}_x$ ceases to decrease. Lengths are scaled with a, velocities with $\langle u \rangle$, forces with $6\pi\eta a \langle u \rangle$, suspension temperature with $(\langle u \rangle a / H)^2$, and stresses with $\eta \langle u \rangle / H$, where η is the fluid viscosity.

3.2.1. *Influence of particle buoyancy.* We present in figure 2 the particle fraction, velocity, and suspension temperature profiles in the fully-developed flow for simulations at $H/a = 30.54$, $\phi_A^b = 0.4$, and $B = 0, 3.4, 11.7$, and 16.8 (simulations A, B, C, and D in order of increasing B). The profiles for the neutrally-buoyant suspension in simulation A are essentially symmetric about the channel centerline, with large ϕ_A near the center of the channel caused by shear-induced particle migration. For $B > 0$, settling and migration compete in the lower half of the channel to yield a heavy-over-light stratification in simulations B, C, and D; adjacent to the upper wall, settling and migration both drive particles down leading to a clear fluid layer. On average, $\bar{h}_x$ decreases as B increases, indicating that particles lie progressively closer to the lower wall. Note, however that the maximum in ϕ_A is at $y > 0.5$ for simulations B, C, and D, while in the neutrally-buoyant case A, ϕ_A has a maximum at $y = 0.5$. The large values of ϕ_A near the centerline in simulation A are reduced at nonzero B. This is because ϕ_A is increased near the lower wall, and hence there is a stronger interaction between suspension and wall. This interaction of the suspension with the wall generates fluctuational motion which loosens the particle packing. Figure 2(c) shows that this reduction of ϕ_A near the center of the channel lessens the blunting of the velocity profile.

For $B > 0$, it is a general result that the maximum velocity occurs above the channel centerline, because the increase in ϕ_A at the bottom of the channel results in increased effective viscosity. Hence, $\dot{\gamma}$ is reduced and the approach to the maximum from the lower wall of the channel is slower than from the upper.

At nonzero B, there are no particles immediately adjacent to the upper wall and T, measured only over the particles, drops to zero here. Though there certainly remains fluctuational motion in the fluid, this is not sampled by our method. In the lower portion of the channel, the region where T exceeds unity widens, while the maximum T grows as gravity is increased. This may be attributed to the increase in both suspension–wall and particle–particle interaction as ϕ_A increases.

3.2.2. *Influence of particle fraction.* We present in figure 3 profiles of ϕ, u, and T in the fully-developed flow at $B = 11.7$ and $H/a = 30.54$ for $\phi_A^b = 0.2, 0.4$, and 0.6 (simulations E, C, and F in order of increasing ϕ_A^b). The flow behavior depends strongly upon ϕ_A^b as shown by figure 3(a). The particles have sedimented into a sheared layer at $\phi_A^b = 0.2$ (simulation E) with shear rate, ϕ_A and T all roughly constant within this layer. Surprisingly, ϕ_A for $0 \leqslant y < 0.2$ is larger for simulation E than simulation C. Above $y \approx 0.35$, the particle fraction in simulation E drops rapidly to zero, while in simulation C it increases, indicating that at the value of $B = 11.7$, shear-induced particle migration is important for $\phi_A^b = 0.4$, but has little influence for $\phi_A^b = 0.2$. For both simulations C and F, the maximum in ϕ_A lies above the centerline, so that relatively dense material flows over light, and in both of these simulations, rapid shearing near the lower wall generates larger values of T than in simulation E.

3.2.3. *Influence of channel width.* We present in figure 4 the results of simulations at $\phi_A^b = 0.4$ and $B = 3.4$ for $H/a = 18.32$ (simulation G1) and $H/a = 30.54$ (simulation B). The flow behavior depends weakly upon H/a relative to the dependence upon ϕ_A^b and B. To a good approximation for these and, presumably, larger values of H/a, the suspension may be treated as a continuum. The scaling of B with $(H/a)^2$ (cf. [1]) effectively reduces the influence of buoyancy, as evidenced by the similarity of the profiles from simulations B and G1 of ϕ_A and u in figure 4(a) and (b). The profiles of T in figure 4(c) do, however, show evidence of the finite size of the particles, as smaller values of T at the center of the channel occur for the larger H/a. The region adjacent to the wall where T varies rapidly has a thickness that scales roughly as a/H, with T of simulation G1 reaching

(a)

(b)

(c)
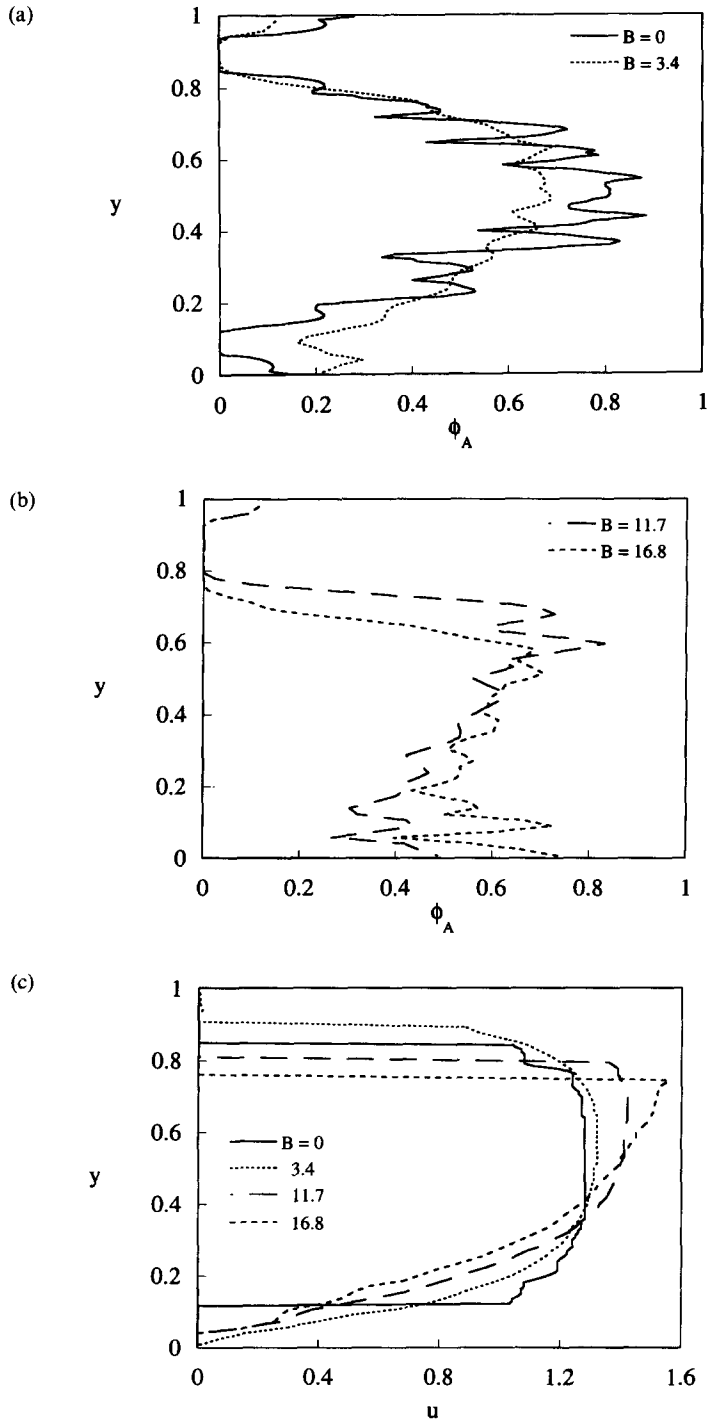
Figures 2(a–c)—*Caption on p.* 000.

a maximum relatively farther from the wall than in the wider channel. These observations are consistent with the findings of NB for the influence of H/a for $B = 0$.

3.2.4. *Simulation parameters: monolayer separation and size of the unit cell.* The influence of separation between monolayers and the size of the simulational unit cell for fixed ϕ_A^b and H/a were investigated. This work was motivated by the observation of NB that, with other parameters held constant, T was systematically larger for larger N. The unit cell is periodically replicated in all directions, so that if the cell is one particle diameter in thickness, particles essentially form cylinders
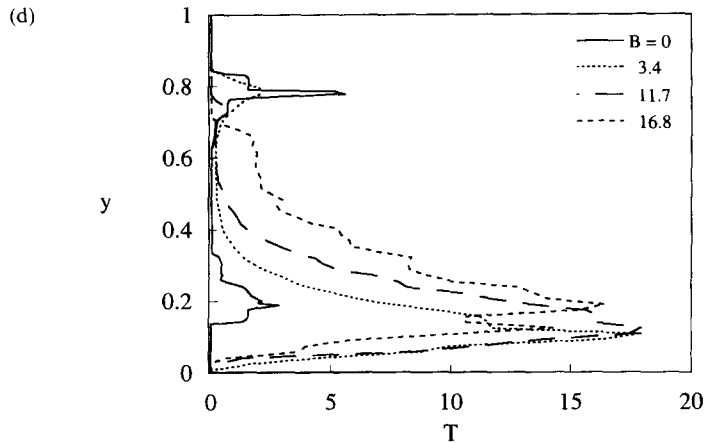
Figure 2. Profiles of the (a and b) particle area fraction ϕ_A, (c) particle velocity u, and (d) suspension temperature T, for $\phi_A^b = 0.4$, $H/a = 30.54$, and $B = 0$, 3.4, 11.7 and 16.8 (simulations A, B, C, and D, respectively).

in the direction perpendicular to the plane of motion. This quasi-two-dimensionality was considered a potential source of the anomalous dependence of T upon N. Increasing the width of the unit cell in this direction while maintaining the restriction of particle motion to the plane of the monolayer breaks this geometrical feature, yet we find the dependence of T upon N remains, and is still unexplained. Fully three-dimensional simulations of channel flows could determine whether constraining the motions of particles to the plane of the monolayer is the cause of the dependence of T upon system size.

A summary of the results of varying N and the monolayer spacing is presented in figure 5, which compares the results of simulations G1, G2, and H. In simulation G2, the monolayers of suspension were separated by a clear fluid layer of four particle radii, while in simulation G1, particles are directly adjacent to their nearest images in the z-direction. Simulation H has particles directly adjacent to their images in the z-direction, but there are 102 particles in the unit cell, rather than 51 as in G1. (The unit cell of simulation H is twice the length in the flow direction but otherwise identical to the unit cell of simulation G1.) The conditions for each simulation are $B = 3.4$, $\phi_A^b = 0.4$, and $H/a = 18.32$. The only systematic difference in u and ϕ_A in these simulations is a slightly smaller u over the entire channel in simulation G2. In figure 5(c), we observe that T of simulation H is larger over the entire channel than in simulations G1 and G2, with the difference most pronounced near the peaks in T. Simulations G1 and G2 show no systematic difference in the value of the suspension temperature, and the dependence of T upon N is thus not explained by the monolayers lying directly adjacent to one another.

The difference in the velocity profiles of simulations G1 and G2 is due simply to the fact that resistance to flow is less within the clear fluid than in the suspension layers. The clear fluid is lower in viscosity and, on average, farther from the fixed wall particles than the monolayers of suspension. Hence, at a given x and y, the velocity is larger in the clear fluid than in the suspension layers, yet the entire velocity field satisfies the prescribed $\langle u \rangle$.

4. SUSPENSION FLOW MODELING

The suspension-balance model outlined by NB was used to predict the fully-developed flow, with model predictions presented together with results of simulations at the same conditions to facilitate evaluation of the success of the model. We also present model predictions for conditions that were not simulated.

4.1. Balance equations and constitutive laws

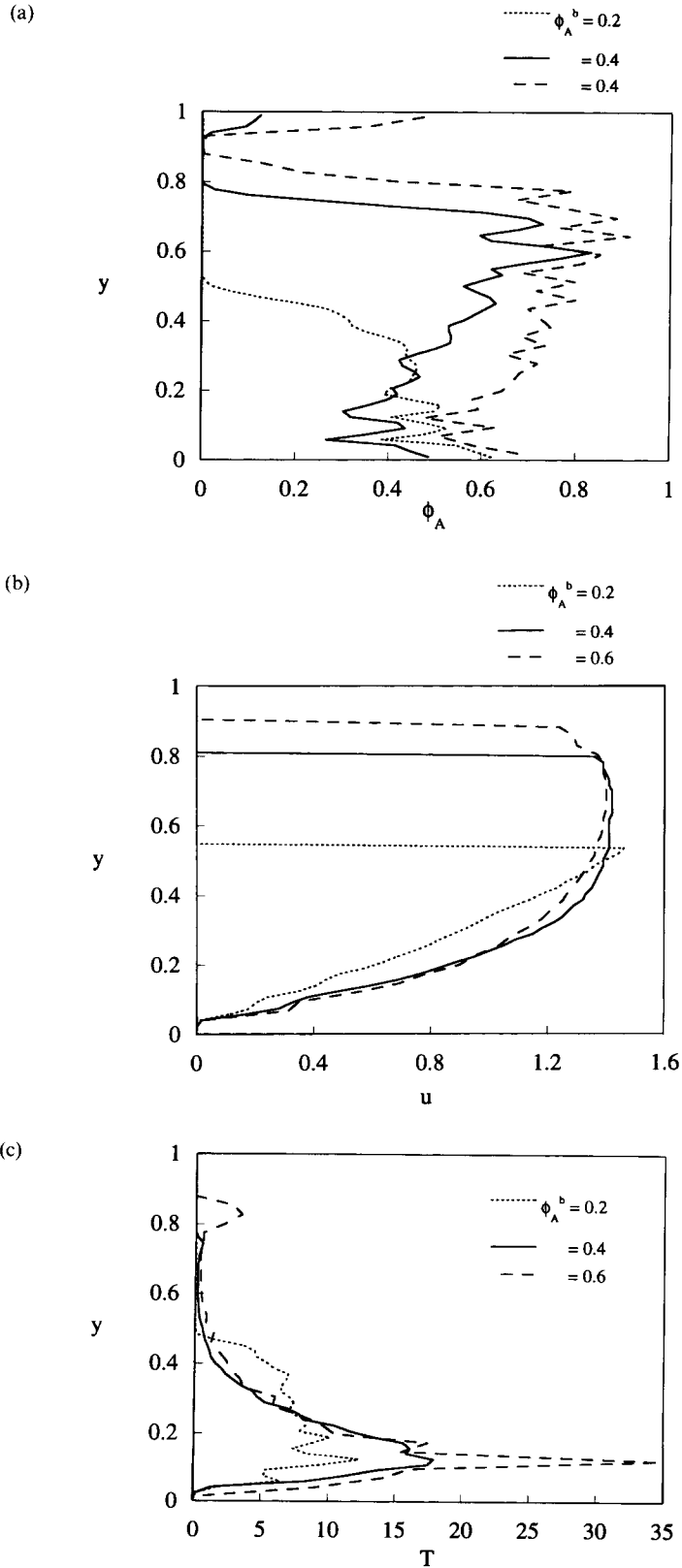Following the derivation in NB, we have the conservation of mass and momentum for the particle phase

Figure 3. Profiles of the (a) particle area fraction ϕ_A, (b) particle velocity u, and (c) suspension temperature T, for $B = 11.7$, $H/a = 30.54$, and $\phi_A^b = 0.2$, 0.4, and 0.6 (simulations E, C, and F, respectively).
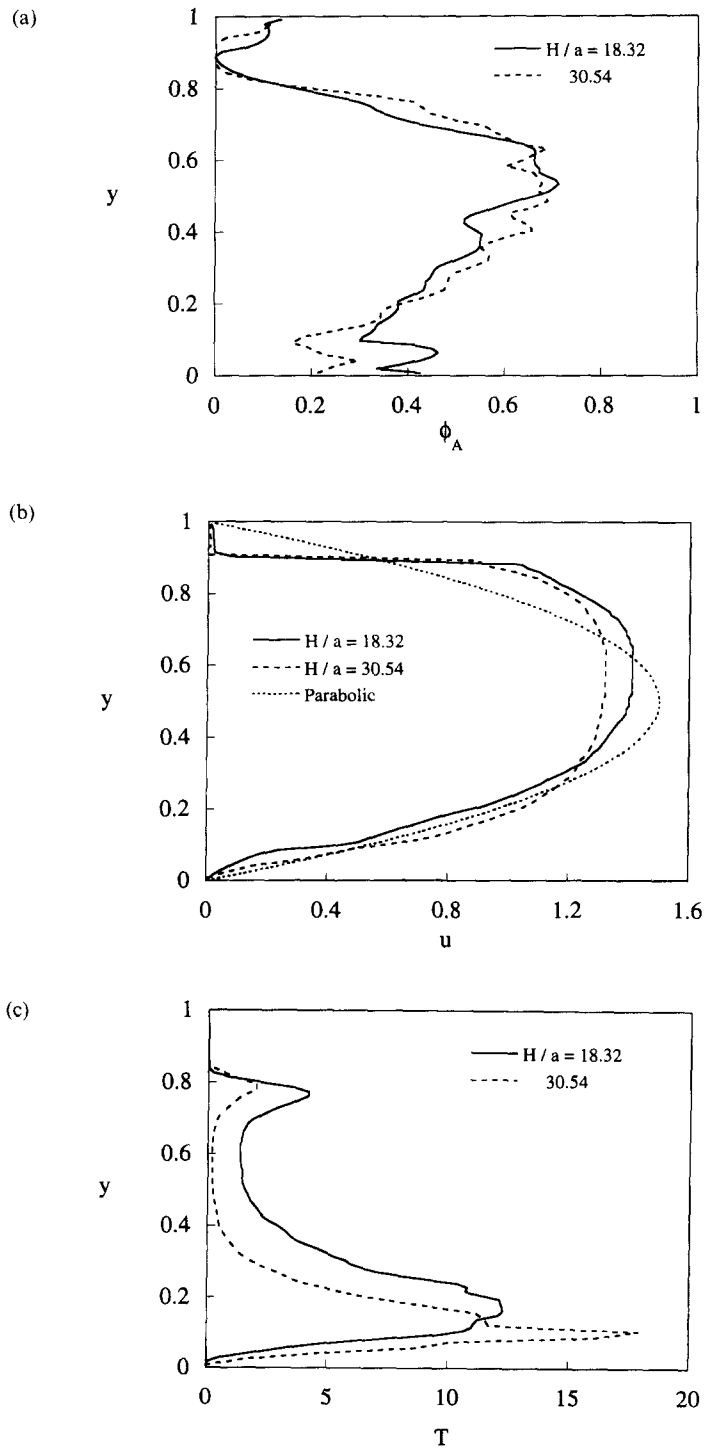
Figure 4. Profiles of the (a) particle area fraction ϕ_A, (b) particle velocity u, and (c) the suspension temperature T, for $\phi_A^b = 0.4$, $B = 3.4$, $H/a = 18.32$ and $H/a = 30.54$ (simulations G1 and B, respectively). The parabolic velocity profile of a Newtonian fluid at the same volumetric flux is shown in (b).
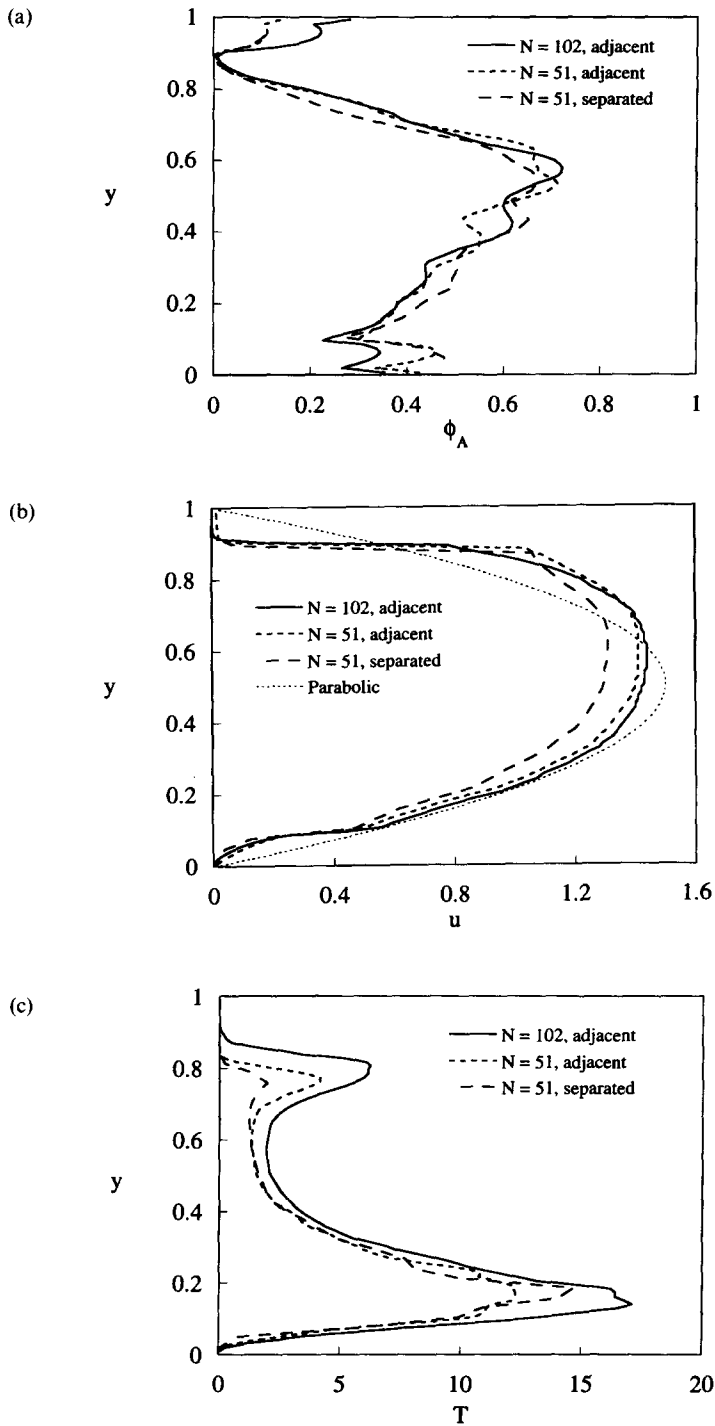
Figure 5. Profiles of the (a) particle area fraction ϕ_A, (b) particle velocity u, and (c) suspension temperature T, for simulations at $\phi_A^b = 0.4$, $B = 3.4$, and $H/a = 18.32$. The simulations differ in the number of particles in the unit cell N, and the separation between the suspension monolayers: monolayers in G1 ($N = 51$) and H ($N = 102$) are directly adjacent; monolayers in G2 ($N = 51$) are separated by a clear fluid layer of thickness four particle radii. The parabolic velocity profile of a Newtonian fluid at the same volumetric flux is shown in (b).

$$\frac{\partial \phi}{\partial t} + \nabla \cdot \phi \langle \mathbf{u} \rangle_p = 0 \tag{8}$$

and

$$\rho_p \phi \frac{D_p \langle u \rangle_p}{Dt} = \langle \mathbf{b} \rangle_p + \langle \mathbf{F} \rangle_p + \nabla \cdot \langle \mathbf{\Sigma} \rangle_p, \tag{9}$$

respectively, where the material derivative in [9] follows the particles $D_p/Dt = \partial/\partial t + \langle \mathbf{u} \rangle_p \cdot \nabla$, with $\langle \mathbf{u} \rangle_p$ the particle-phase average velocity; $\langle \cdot \rangle_p$ denotes a particle-phase average. Also, in [9], $\langle \mathbf{b} \rangle_p$, $\langle \mathbf{F} \rangle_p$, and $\langle \mathbf{\Sigma} \rangle_p$ are the average body force, hydrodynamic force, and stress of the particle phase, respectively.

The suspension-averaged velocity $\langle \mathbf{u} \rangle$ is needed, for example, in the expression for $\langle \mathbf{F} \rangle_p$. This velocity is governed by the ensemble average of the mass and momentum conservation equations, taken over all points in the suspension. For incompressible materials, these equations are

$$\nabla \cdot \langle \mathbf{u} \rangle = 0 \tag{10}$$

and

$$\frac{D \langle \rho \mathbf{u} \rangle}{Dt} = \langle \mathbf{b} \rangle + \nabla \cdot \langle \mathbf{\Sigma} \rangle, \tag{11}$$

where the material derivative in this case, $D/Dt = \partial/\partial t + \langle \mathbf{u} \rangle \cdot \nabla$, follows the suspension-averaged motion. We now discuss the various quantities in [8]–[11] and present the constitutive models used.

We are interested in the case where the particle density differs from that of the fluid. In [9], $\langle \mathbf{b} \rangle_p = (\rho_p - \rho_f) \mathbf{g} \phi$: although the average body force on the particles per unit volume is $\rho_p \mathbf{g} \phi$, only the differential body force is relevant to the particle dynamics, as a constant body force $\rho_f \mathbf{g}$ at all points can be absorbed into a linearly varying pressure which is hydrostatically stable.

The average hydrodynamic force per unit volume on the particle phase $\langle \mathbf{F} \rangle_p$ is given by the low-Reynolds-number expression in terms of the resistance tensor and the particle velocity relative to the suspension average

$$\begin{aligned} \langle \mathbf{F} \rangle_p &= -n \langle \mathbf{R}_{FU} \cdot (\mathbf{u} - \langle \mathbf{u} \rangle) \rangle_p \\ &\approx -n \langle \mathbf{R}_{FU} \rangle_p \cdot (\langle \mathbf{u} \rangle_p - \langle \mathbf{u} \rangle) \\ &\approx -6 \pi \eta a n f(\phi)^{-1} (\langle \mathbf{u} \rangle_p - \langle \mathbf{u} \rangle), \end{aligned} \tag{12}$$

where n is the particle number density. In obtaining the second and third lines in [12], we have broken the average of $\langle \mathbf{R}_{FU} \cdot \mathbf{u} \rangle_p$ and assumed that the average resistance tensor is isotropic. The hindered settling function, $f(\phi)$, is the ratio of the settling velocity of a particle in bulk sedimentation relative to the Stokes settling velocity of an isolated particle; $f(\phi)$ has been measured experimentally (see the review by Davis & Acrivos (1985)) and evaluated by Stokesian Dynamics simulation (Phillips et al. 1988).

We can now see how migration arises in the context of this model. For vanishing Reynolds number, the LHS of [9] is zero, and if we consider the case of neutrally buoyant particles, [12] and [9] taken together indicate that the particle flux $\phi \langle \mathbf{u} \rangle_p$ appearing in [8] is given by

$$\phi \langle \mathbf{u} \rangle_p = \phi \langle \mathbf{u} \rangle + \frac{2a^2}{9\eta} f(\phi) \nabla \cdot \langle \mathbf{\Sigma} \rangle_p, \tag{13}$$

where we have used $\phi = (4\pi/3)a^3 n$. Motion relative to the suspension average is driven by stress gradients—that is, stress-induced migration. Furthermore, it is the normal stresses that are responsible for cross-stream migration. Considering flow in the x-direction with variations only in the y-direction, the cross-stream flux in [13] is driven by

$$(\nabla \cdot \mathbf{\Sigma})_y = \frac{\partial \Sigma_{yy}}{\partial y}. \tag{14}$$

The conclusion is that non-Newtonian normal stresses are responsible for the migration. This is in marked contrast to the modeling of Leighton & Acrivos (1987b) and Phillips et al. (1992) in

which the suspension is assumed Newtonian and the particle migration is postulated to result from variation in shear stress (or shear rate).

The particle contribution to the suspension stress (Brady 1993, NB) is given by

$$\langle \Sigma \rangle_p = \langle S \rangle_p + \tfrac{1}{2} \epsilon \cdot \langle L^{ext} \rangle_p - \langle x'b' \rangle_p - \tfrac{1}{2} \rho_p \langle ra + ar \rangle_p - \rho_p \langle u'u' \rangle_p. \qquad [15]$$

In [15], $\langle S \rangle_p$ is the hydrodynamic stresslet; $-\langle x'b' \rangle_p$ is the stress due to nonhydrodynamic interparticle forces; $-\rho_p \langle u'u' \rangle_p$ is the particle contribution to the inertial Reynolds stress; $\tfrac{1}{2}\epsilon \cdot \langle L^{ext} \rangle_p$ is the antisymmetric stress that results from the application of an external torque $\langle L^{ext} \rangle_p$ upon the particles, with ϵ the unit alternating tensor; and the stress resulting from the moment about the particle centers ($r = x - x'$, with x' the center of the ith particle) of the local acceleration is $-(\rho_p/2)\langle ra + ar \rangle_p$. The hydrodynamic stresslet (Batchelor 1970) is given for rigid particles by

$$S_i = \frac{1}{2} \int_{A_i} [r\sigma \cdot n + \sigma \cdot nr] \, dA,$$

where n is the normal projecting out of the particle and A_i is the surface of particle i; note that, in general, S_i is not traceless. The stresslet is a continuum mechanical concept, and is the only stress contribution without a direct counterpart in the expression for the stress in a molecular system for molecules of finite size (Irving & Kirkwood 1950).

No external torque is applied to the particles, and we consider low-Reynolds-number flows, so that both the acceleration and Reynolds stresses are negligible. Thus, the constitutive law for the particle stress for rectilinear flows takes the form

$$\langle S \rangle_p = -\Pi(\phi)I + 2\eta\eta_p(\phi)\langle e \rangle, \qquad [16]$$

in which Π is the particle contribution to the pressure, $\eta_p = \eta_s - 1$ is the particle viscosity made dimensionless with the fluid viscosity, and $\langle e \rangle$ is the bulk rate of strain. In general, normal stress differences must be included in [16] as discussed by NB and Brady and Morris (1997), but can be omitted here because normal stress differences play no role in the fully-developed flow in a straight channel; normal stress differences are important in curvilinear flows.

It was shown by Jeffrey *et al.* (1993) that the hydrodynamic contribution to the particle pressure could be written as

$$\Pi = -\tfrac{1}{3} I : \langle S \rangle_p = \langle P \cdot (u - \langle u \rangle) - Q : \langle e \rangle \rangle_p, \qquad [17]$$

in which P_i and Q_{ij} are the hydrodynamic resistance tensors relating particle velocity and the bulk rate of strain to the isotropic stress, respectively.

On dimensional grounds, the particle pressure, or any stress, in a low-Reynolds-number flow should have the form

$$\Pi = \eta\dot{\gamma}\mathscr{F}(\phi, a/H), \qquad [18]$$

where $\dot{\gamma}$ is a measure of the local shear rate $\dot{\gamma} = \sqrt{\langle e \rangle : \langle e \rangle}$ and $\mathscr{F}(\phi, a/H)$ is a nondimensional function of volume fraction and a/H. At steady state the y-particle flux [13] is zero, and thus from [14] $\partial \Sigma_{yy}/\partial y = \partial \Pi/\partial y = 0$. Hence, from [18] we see that if $\dot{\gamma}$ varies, as in pressure-driven flow, then ϕ must vary so as to keep the normal stress constant; where $\dot{\gamma}$ is large, ϕ is small and vice versa. Here we are assuming that $\mathscr{F}(\phi)$ is a monotonically increasing function of ϕ and that $a/H \ll 1$ so that it does not influence the behavior.

In a homogeneous shear flow, $a/H \equiv 0$ and $\Pi = \eta\dot{\gamma}\mathscr{F}(\phi)$ gives a complete description of the stress. In an inhomogeneous flow, however, it may be necessary to take into account the variation of Π with a/H as in [18] even though a/H is small; that is, a nonlocal expression for the stress may be needed. For example, a finite pressure can exist even in regions where the macroscopic shear rate is zero because the local fluctuational motion $u' = u - \langle u \rangle$ can be nonzero, and from [17] nonzero fluctuational motion can generate a pressure. To capture this important feature and construct a simple nonlocal expression for the pressure, we model the pressure as dependent upon

the fluctuational motion, given by $T = \langle \mathbf{u}' \cdot \mathbf{u}' \rangle$, akin to the treatment of granular flows and first suggested by Jenkins and McTigue (1990) for use in suspension mechanics

$$\Pi = \eta a^{-1} p(\phi) \sqrt{T}, \qquad\qquad [19]$$

in which Π is proportional to the square root of the suspension temperature (and hence linear in velocity) because it is a viscously-generated stress. Here $p(\phi)$ is a nondimensional function of solids concentration.

As will be seen from the energy balance [25] discussed below, in a homogeneous flow T is directly proportional to $\langle \mathbf{e} \rangle : \langle \mathbf{e} \rangle$, and writing the pressure in terms of T or $\langle \mathbf{e} \rangle$ (i.e. in terms of $\dot{\gamma}$) is entirely equivalent. In an inhomogeneous flow, however, the fluctuational motion is not necessarily strictly proportional to $\langle \mathbf{e} \rangle$, and need not vanish when $\langle \mathbf{e} \rangle$ vanishes. A pressure proportional to $\langle \mathbf{e} \rangle$ will vanish at the velocity maximum in pressure-driven flow and lead to $\phi = \phi_m$ at this point regardless of the bulk particle fraction. This behavior is removed by writing pressure in terms of T, as the energy balance for T introduces a nonlocality for the stress as discussed below.

The expression for the suspension stress is of the same form as [15] for the particle stress, with averaging now over the entire suspension. The constitutive law for the suspension stress is, again for rectilinear motion, thus

$$\langle \mathbf{\Sigma} \rangle = -\langle p \rangle_f \mathbf{I} + 2\eta \langle \mathbf{e} \rangle + \langle \mathbf{\Sigma} \rangle_p$$

$$= -(\Pi + \langle p \rangle_f)\mathbf{I} + 2\eta \eta_s(\phi)\langle \mathbf{e} \rangle, \qquad\qquad [20]$$

where $\langle p \rangle_f$ is the average pressure in the fluid and η_s is the relative viscosity of the suspension.

To determine the pressure in [19], we must determine T. An equation governing T is deduced from a consideration of the kinetic energy balance for the entire suspension. Taking the suspension average of the equation resulting from the scalar product of $\mathbf{u}$ with Cauchy's equation, and subtracting from this equation the scalar product of $\langle \mathbf{u} \rangle$ with the average momentum equation for the suspension [11] yields (Batchelor 1970)

$$\frac{D\langle \rho(u')^2 \rangle}{Dt} = \langle \mathbf{b}' \cdot \mathbf{u}' \rangle + \langle \mathbf{\Sigma} \rangle : \langle \mathbf{e} \rangle - \langle \dot{\Phi} \rangle - \nabla \cdot \langle \mathbf{\Sigma}' \cdot \mathbf{u}' \rangle. \qquad\qquad [21]$$

On the right-hand side of [21], $\langle \mathbf{b}' \cdot \mathbf{u}' \rangle$ and $\langle \mathbf{\Sigma} \rangle : \langle \mathbf{e} \rangle$ represent the rates of working by fluctuating interparticle and body forces and by the mean bulk stress, respectively; $\langle \dot{\Phi} \rangle$ is the average rate of viscous dissipation of mechanical energy into heat, and the final term is the divergence of the flux vector of microscale fluctuational motion.

Equation [21] is used to motivate the form of the equation governing T. The dissipation rate for a low-Reynolds-number suspension is given by (Brady & Bossis 1988)

$$\dot{\Phi} = \begin{pmatrix} \mathbf{u} - \langle \mathbf{u} \rangle \\ -\langle \mathbf{e} \rangle \end{pmatrix} \cdot \begin{bmatrix} \mathbf{R}_{FU} & \mathbf{R}_{FE} \\ \mathbf{R}_{SU} & \mathbf{R}_{SE} \end{bmatrix} \cdot \begin{pmatrix} \mathbf{u} - \langle \mathbf{u} \rangle \\ -\langle \mathbf{e} \rangle \end{pmatrix}. \qquad\qquad [22]$$

The dissipation consists of a term $\langle \mathbf{u}' \cdot \mathbf{R}_{FU} \cdot \mathbf{u}' \rangle$, due to fluctuational motion of the particles relative to the local mean motion, a term $\langle \mathbf{e} \rangle : \langle \mathbf{R}_{SE} \rangle : \langle \mathbf{e} \rangle$ due to the particles moving "affinely" with the average bulk motion and terms due to coupling of the fluctuational and bulk motions. The fluctuational dissipation is proportional to the suspension temperature

$$\langle \mathbf{u}' \cdot \mathbf{R}_{FU} \cdot \mathbf{u}' \rangle \sim 6\pi\eta a f(\phi)^{-1} T, \qquad\qquad [23]$$

a fact that is used to model the dissipation as proportional to T, By introducing a Newtonian constitutive law for the stress, the flux vector appears in a form which suggests modeling by a Fourier law

$$-\langle \mathbf{\Sigma}' \cdot \mathbf{u}' \rangle \sim -\eta \eta_p \langle \nabla \mathbf{u}' \cdot \mathbf{u}' \rangle \sim -\eta \kappa(\phi)\nabla T, \qquad\qquad [24]$$

in which the "conductivity" coefficient $\kappa(\phi)$ is proportional to the particle viscosity $\eta_p(\phi)$. We discard the dissipation due to affine motion as this would be present in an ordered system and does

not generate fluctuational motion, and use the constitutive models expressed by [23] and [24] to pose the following equation for the particle fluctuational motion:

$$c(\phi)\frac{DT}{Dt} = \beta(\phi)\langle\mathbf{b}'\cdot\mathbf{u}'\rangle + \langle\mathbf{\Sigma}\rangle_{\mathrm{p}}:\langle\mathbf{e}\rangle - \eta\alpha(\phi)a^{-2}T - \nabla\cdot\kappa(\phi)\nabla T. \qquad [25]$$

Keeping the rate of working unchanged while discarding the affine dissipation requires introduction of phenomenological coefficients: $c(\phi)$ is analogous to a heat capacity, $\alpha(\phi)$ describes the magnitude of T in homogeneous shear flow, and $\beta(\phi)$ together with $\alpha(\phi)$ gives T in a homogeneous sedimentation. The average particle stress $\langle\mathbf{\Sigma}\rangle_{\mathrm{p}}$ appears on the right of [25] because the fluid dissipation is associated with the discarded affine motion.

From [25] one can readily see that in a homogeneous shear flow, where $\nabla T = 0$, T is directly proportional to $\langle\mathbf{e}\rangle:\langle\mathbf{\Sigma}\rangle_{\mathrm{p}}\propto\langle\mathbf{e}\rangle:\langle\mathbf{e}\rangle$; thus, writing the pressure in terms of $\dot\gamma$ or $\sqrt{T}$ is entirely equivalent. In an inhomogeneous flow, however, $\nabla T \neq 0$ and the flux of fluctuational energy will cause T to be nonzero even if $\dot\gamma$ is zero. Further, if one assumes ∇T is small and expands for T from [25], Π will be nonlocal in $\dot\gamma$ and ϕ, with terms proportional to $\nabla\dot\gamma$, $\nabla\phi$, and higher-order gradients present.

Closure of the governing equations requires specification of the ϕ-dependent functions η_s, p, c, α, β, and κ. For the suspension viscosity, we take

$$\eta_{\mathrm{s}}(\phi) = \left(1 - \frac{\phi}{\phi_{\mathrm{m}}}\right)^{-2}, \qquad [26]$$

which differs only through the exponent of -2 (rather than -1.82) from Krieger's (1972) correlation of experimental data, and the particle viscosity is given by $\eta_{\mathrm{p}} = \eta_{\mathrm{s}} - 1$. The exponent -2 is suggested by the theory of Brady and Morris (1997). The other ϕ-dependent functions, all recently defined by NB, can be determined from independent experiments or simulations. In fact, all except the "conductivity" coefficient $\kappa(\phi)$ can be determined from experiments at homogeneous conditions. This work has yet to be performed, however, and the coefficients used here are modeled.

The pressure function is recommended by NB as

$$p(\phi) = \phi^{1/2}\eta_{\mathrm{p}}(\phi) \qquad [27]$$

with the leading $\phi^{1/2}$ included so that as $\phi \to 0$, $\Pi = O(\phi^2)$ (T is proportional to ϕ as $\phi \to 0$), in agreement with the analysis of Jeffrey et al. (1993). The factor of $\phi^{1/2}$ was omitted here, taking $p(\phi) = \eta_{\mathrm{p}}(\phi)$.

The coefficients in the equation governing T are taken as

$$\alpha(\phi) = \frac{k_\alpha\eta_{\mathrm{p}}(\phi)}{\phi} \quad \text{and} \quad \kappa(\phi) = k_\kappa\eta_{\mathrm{p}}(\phi), \qquad [28]$$

where k_α and k_κ are constants. The coefficient $c(\phi)$ is not needed here because we consider only fully-developed flow; $\beta(\phi)$ is also not needed because there is no average phase slip in the fully-developed flow.

The model equations are made dimensionless by scaling lengths with H, velocities with $\langle\mathbf{u}\rangle \sim |\nabla\langle P\rangle|H^2/\eta$, and T with $(a/H)^2\langle u\rangle^2$. We define $\epsilon \equiv a/H$. For steady, fully-developed channel flow variations are only in the cross-stream y-direction, and the dimensionless particle momentum balances are

$$\frac{\mathrm{d}}{\mathrm{d}y}\left(\eta_{\mathrm{p}}(\phi)\frac{\mathrm{d}\langle u_x\rangle}{\mathrm{d}y}\right) = -\phi + \frac{9}{2}\epsilon^{-2}\phi f^{-1}(\phi)(\langle u_x\rangle_{\mathrm{p}} - \langle u_x\rangle) \qquad [29]$$

and

$$\frac{\mathrm{d}}{\mathrm{d}y}\left(p(\phi)\sqrt{T}\right) = -B\phi, \qquad [30]$$

where the $-\phi$ on the RHS of [29] is the scaled form of the particle-phase average of the constant pressure gradient, and B is the buoyancy parameter defined by [1]. An immediate simplification is obtained by assuming $\epsilon^2 \ll 1$, an assumption consistent with describing the particulate phase as an

effective continuum. The particle x-momentum balance [29] is then $\langle u_x \rangle_p = \langle u_x \rangle + O(\epsilon^2)$: in the fully-developed flow, there is negligible slip between the average particle and suspension average velocities. The equation governing the velocity is thus the x-momentum balance for the entire suspension

$$\frac{d}{dy}\left(\eta_s(\phi)\frac{d\langle u_x\rangle}{dy}\right) = -1,$$ [31]

where the -1 on the RHS is the scaled constant pressure gradient. At steady state, the equation governing T is

$$\eta_p(\phi)\left(\frac{d\langle u\rangle}{dy}\right)^2 - \alpha(\phi)T + \epsilon^2\frac{d}{dy}\left(\kappa(\phi)\frac{dT}{dY}\right) = 0.$$ [32]

Here and in the following, we omit the subscript x on the velocity. We carry out the differentiation in [30] to yield

$$p'\frac{d\phi}{dy} + \frac{p}{2T}\frac{dT}{dy} = \frac{-B\phi}{\sqrt{T}},$$ [33]

where $p' = dp/d\phi$. This equation is linear in T for $B = 0$, but nonlinear for $B > 0$. Particle buoyancy introduces a new type of nonlinearity to the model equations, with the other nonlinearity (in ϕ) being due to the ϕ-dependent coefficients.

The boundary conditions should be derived in a manner analogous to the governing equations. This has not been done, however, and we simply model the boundary conditions in the simplest possible manner. We have no slip at both walls

$$\langle u\rangle = 0 \quad \text{at} \quad y = 0 \quad \text{and} \quad y = 1$$ [34]

while the particle fraction must sum to the bulk value

$$\int_0^1 \phi_A(y)\,dy = \phi_A^b.$$ [35]

The conditions on T prove to be more problematic. Simulations and a consideration of the hydrodynamic interactions of particles with the walls suggest that the boundary condition should be $T \approx 0$ at the walls. However, NB showed that with the present constitutive model of the stress this required $\phi = \phi_m$, the maximum packing fraction, at the wall to generate the finite particle pressure necessary to satisfy the y-momentum balance. Here, we apply an ad hoc condition intended to reflect in a simple fashion the hydrodynamic damping of fluctuational motion by the wall. The condition is

$$T_w = \frac{\eta_p(\phi_w)}{\alpha^*}\left(\frac{d\langle u\rangle}{dy}\right)^2 \quad \text{at} \quad y = 0 \quad \text{and} \quad y = 1,$$ [36]

where the subscript w indicates the limiting value as the wall is approached from the suspension, and α^* is larger than $\alpha(\phi_w)$ by an arbitrarily chosen factor of 20. In essence, the wall is represented as a region of particles near maximum packing, which allows T to be small but finite at the wall. This yields good agreement with simulation results. The coupled set of ordinary differential equations [30]–[32] are solved subject to the conditions [34]–[36] for ϕ, $\langle u\rangle$, and T.

To generate model predictions for comparison with the simulational results, the constitutive equations are modified for use in determining the area fraction ϕ_A. As shown by NB, the constitutive equations reported above are satisfactory for use in predicting area fraction if ϕ and ϕ_m are replaced by ϕ_A and $\phi_{A,m}$ where $\phi_{A,m}$ is the maximum random packing fraction of circles in a plane, determined by Kausch et al. (1971) to be $\phi_{A,m} \approx 0.83$.

A finite-difference scheme is used to solve the second-order [31] and [32] for $\langle u\rangle$ and T, respectively. The y-momentum equation is a first-order equation for ϕ_A, and the linearized

difference equation in the numerical solution is solved analytically using a summing factor (see Bender & Orszag 1978, p. 38) analogous to the integrating factor used for first-order linear differential equations. Simulations show that for sufficiently large B, there is a region without particles adjacent to the upper wall, a result which the continuum equations cannot predict. We set the particle fraction to zero if it falls below 10^{-3}, and find this *ad hoc* method entirely satisfactory. The solution is computed on a one-dimensional grid of 500 nodes.

The set of equations is solved by a nested-iteration algorithm, which begins with the assumption of a particle fraction profile $\phi_A^{(0)}(y)$ having the desired bulk fraction ϕ_A^b. The x-momentum equation is solved using $\phi_A^{(0)}(y)$ for the particle fraction to yield the velocity field $u^{(0)}(y)$. Employing $u^{(0)}(y)$ in the temperature equation, $T^{(0)}(y)$ is determined. The field $T^{(0)}(y)$ is then substituted into the linearized y-momentum equation, which is iterated with systematic increase or decrease of $\phi_A(0)$ until the average particle fraction is ϕ_A^b with the field satisfying this condition denoted $\phi_A^{(1)}(y)$. This nested iteration completes the first overall iteration, and $\phi_A^{(1)}(y)$ is used in the x-momentum equation to begin the second. The procedure is continued until convergence is achieved, with our convergence criterion being that the integrated absolute difference between two subsequent $\phi_A^{(i)}$ is less than one-half of one percent.

4.2. *Model predictions*

In figure 6, the predicted fully-developed flow for $B = 3.4$, $\phi_A^b = 0.4$, and $H/a = 30.54$ is presented together with the results of simulation B, at the same conditions. In order to show the agreement of the predictions with simulation data more clearly, we have omitted the small peak in ϕ_A from simulation which occurs because particles occasionally stick to the upper wall through lubrication forces. The model was fitted to the simulation results at these conditions using k_α and k_κ as fitting parameters, with the appropriate values found to be

$$k_\alpha = 0.815 \quad \text{and} \quad k_\kappa = 0.8, \tag{37}$$

noticeably different from the values of $k_\alpha = 0.19$ and $k_\kappa = 0.17$ used by NB; the values given by [37] were used in all of the modeling reported here. Note that the suspension average velocity, and not the particle-phase average, is predicted by the model, and hence the difference in the velocities in the clear fluid layer above $y \approx 0.82$.

In figure 7, model predictions are compared with simulation results for $\phi_A^b = 0.6$, $H/a = 30.54$, and $B = 8.4$. The bulk particle fraction has increased by 50% and B by a factor of roughly 2.5, but the values of k_α and k_κ were unchanged. For an example of the change in conditions, note that $\eta_s(\phi_A^b)$ increases by a factor of 3.5. Model predictions remain in good agreement with the simulation results. Although prediction of ϕ_A is less accurate than in the prior case, the qualitative features of the flow are captured correctly. In the ϕ_A profile from simulation in figure 7(a), considerable ordering is seen at the channel center, which results from the interparticle repulsive force becoming large compared to the weak shear flow. This behavior cannot be predicted by the model. Because the model assumes smooth shearing of the suspension at all $\phi_A < \phi_{A,m}$, the sticking of particles to the walls observed in the simulation results is an understandable disparity between the predicted and observed u. Remarkably, however, the maximum in T is correctly predicted to lie above the channel centerline.

A composite of the predicted fully-developed flow profiles for $\phi_A^b = 0.4$ and $H/a = 30$ over a range of B is shown in figure 8. Note the large difference between the predicted flows at $B = 25$ and 25.5, and that the maximum in T undergoes nonmonotonic variation with respect to B: the maximum T increases until $B \approx 25$ and then drops dramatically for larger values of B. Apparently, as ϕ_A at the lower wall increases with B, the reduction in shear rate is outstripped by the growth in intensity of particle interactions until $B \approx 25$. Between $B = 17$ and 25, the upper surface of the suspended layer of particles is predicted to fall below the suspension velocity maximum, and for the larger values of B, the majority of the volumetric flux in the channel occurs in the clear fluid layer, with particles transported in a shear layer along the lower wall.

The model does not accurately reflect the reduction in both the maximum particle fraction and degree of blunting as B is increased that was demonstrated by simulations A–D (see figure 2). Figure 8 illustrates that the model predicts only a slight reduction in the maximum ϕ_A in going from $B = 3.4$ to 17, and consequently predicts an almost indiscernible change in the u profiles. It
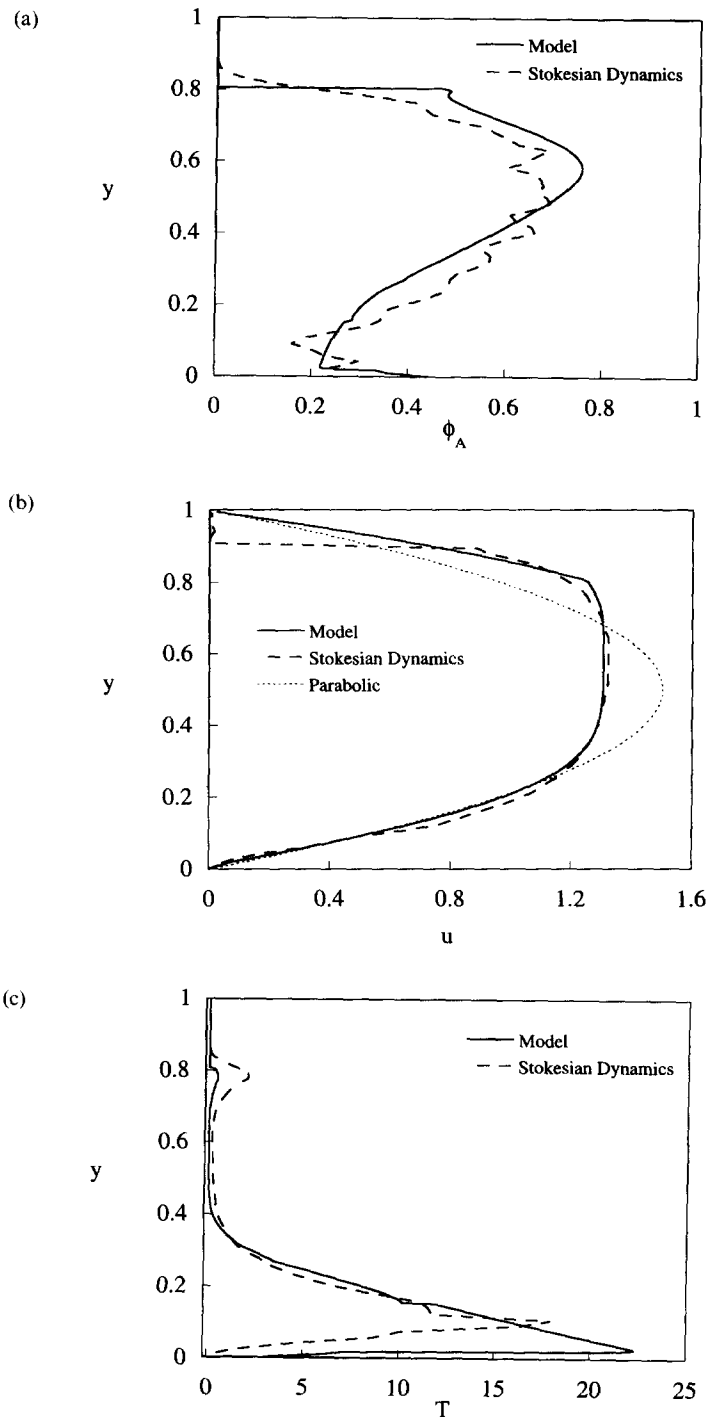
Figure 6. Model predictions and Stokesian Dynamics simulation results for the fully-developed flow of a suspension at $\phi_A^b = 0.4$, $B = 3.4$, and $H/a = 30.54$. Profiles of (a) the particle fraction ϕ_A, (b) the velocity u (of the entire suspension in the case of the model, particles for the simulation), and (c) suspension temperature T are shown. The parabolic velocity profile of a Newtonian fluid at the same volumetric flux is shown in (b).

is possible that this could be remedied by an increase in the value of k_κ, but this would entail also a change in the value of k_α.

Based on agreement of model predictions with simulation results at conditions well-removed from those at which k_κ and k_α were determined, we conclude that the modeled coefficients accurately

capture the ϕ dependence. Thus, we may predict flows for which simulation and experimental data are lacking. This is especially useful for conditions which would be prohibitively time-consuming to simulate. Predictions for the conditions $\phi_A^b = 0.6$, $H/a = 100$, and $B = 5$ are presented in figure 9. The particle fraction is predicted to be close to $\phi_{A,m}$ in a wide layer, with consequent extreme
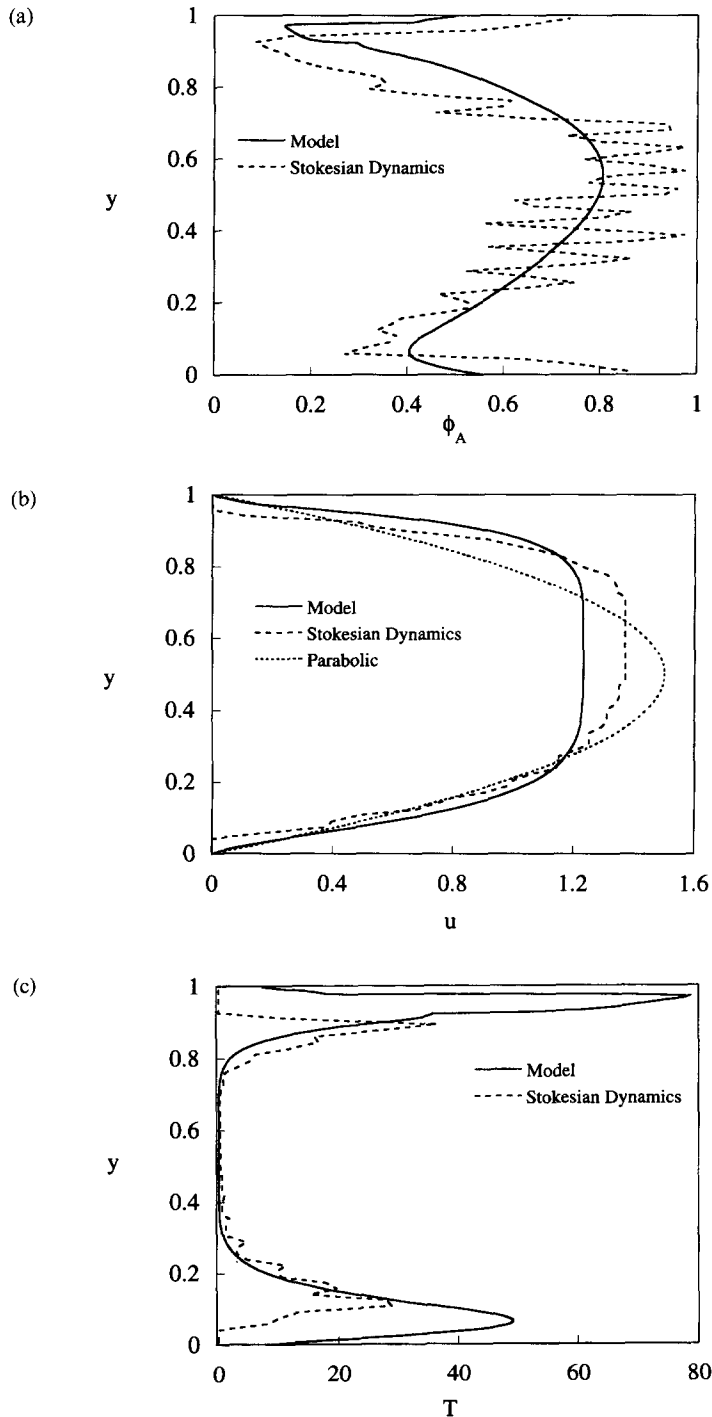

Figure 7. Model predictions and Stokesian Dynamics simulation results for the fully-developed flow of a suspension at $\phi_A^b = 0.6$, $B = 8.4$, and $H/a = 30.54$. Profiles of the (a) particle fraction $\phi/_A$, (b) velocity u (of the entire suspension in the case of the model, particles for the simulation), and (c) suspension temperature T are shown. The parabolic velocity profile of a Newtonian fluid at the same volumetric flux is shown in (b).
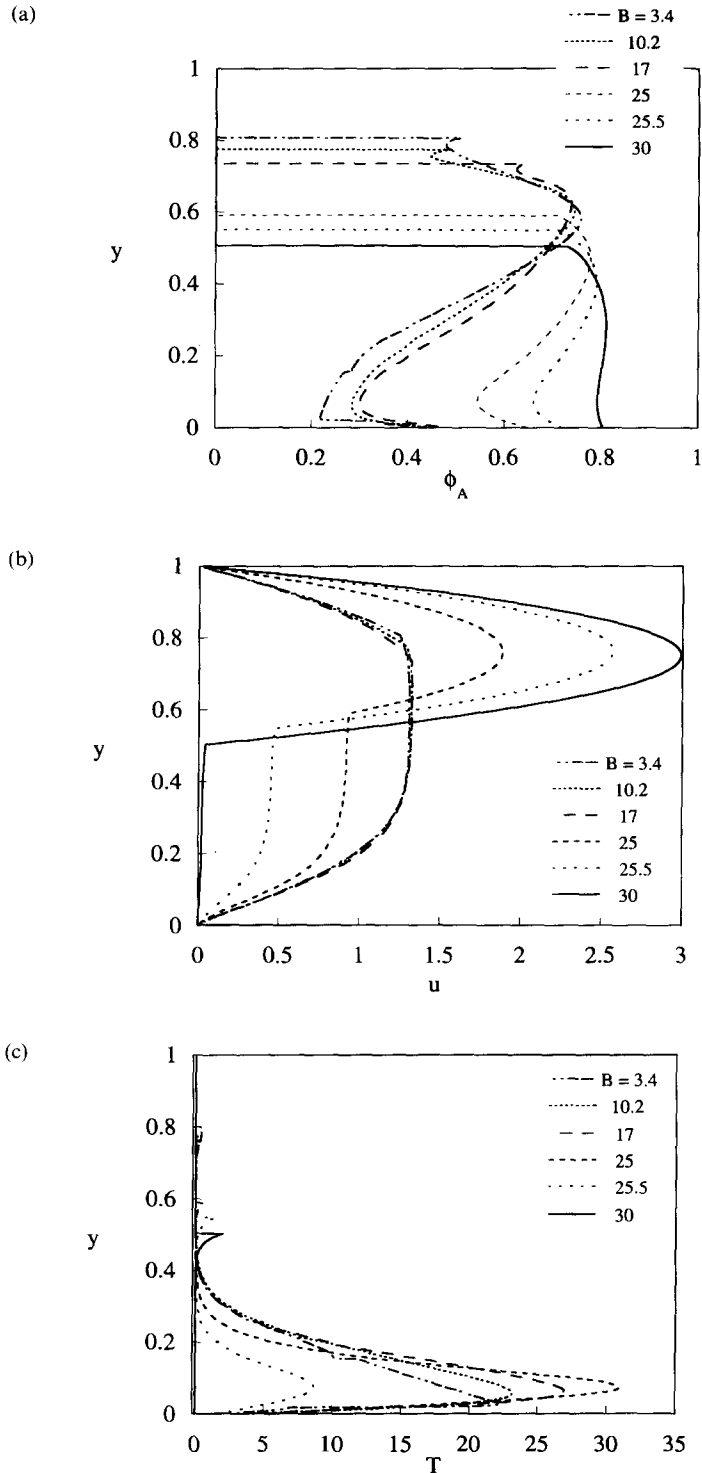
Figure 8. Model predictions for the fully-developed flow of a suspension at $\phi_A^b = 0.4$, $H/a = 30$, and a range of B. Profiles of (a) particle fraction ϕ_A, (b) suspension velocity u, and (c) suspension temperature T are shown.

blunting of the velocity profile and essentially vanishing T. This layer is supported by a rapidly-sheared layer in which ϕ_A is more dilute and T is large.

The model equations converge to legitimate solutions for $\phi_A^b > 0.15$. At smaller particle fractions, the model as implemented in this study typically failed to converge. One possible cause of this

failure is the omission of $\phi^{1/2}$ in the constitutive law $p(\phi) = \phi^{1/2}\eta_p(\phi)$ (see [27]). Further study of the functional forms of $p(\phi)$, $\alpha(\phi)$, and $\kappa(\phi)$ (in particular as $\phi \to 0$) is needed in order to assess whether the cause of difficulty is this omission, inappropriate forms of other coefficients of the model for small ϕ, or the method of solution of the governing equations.
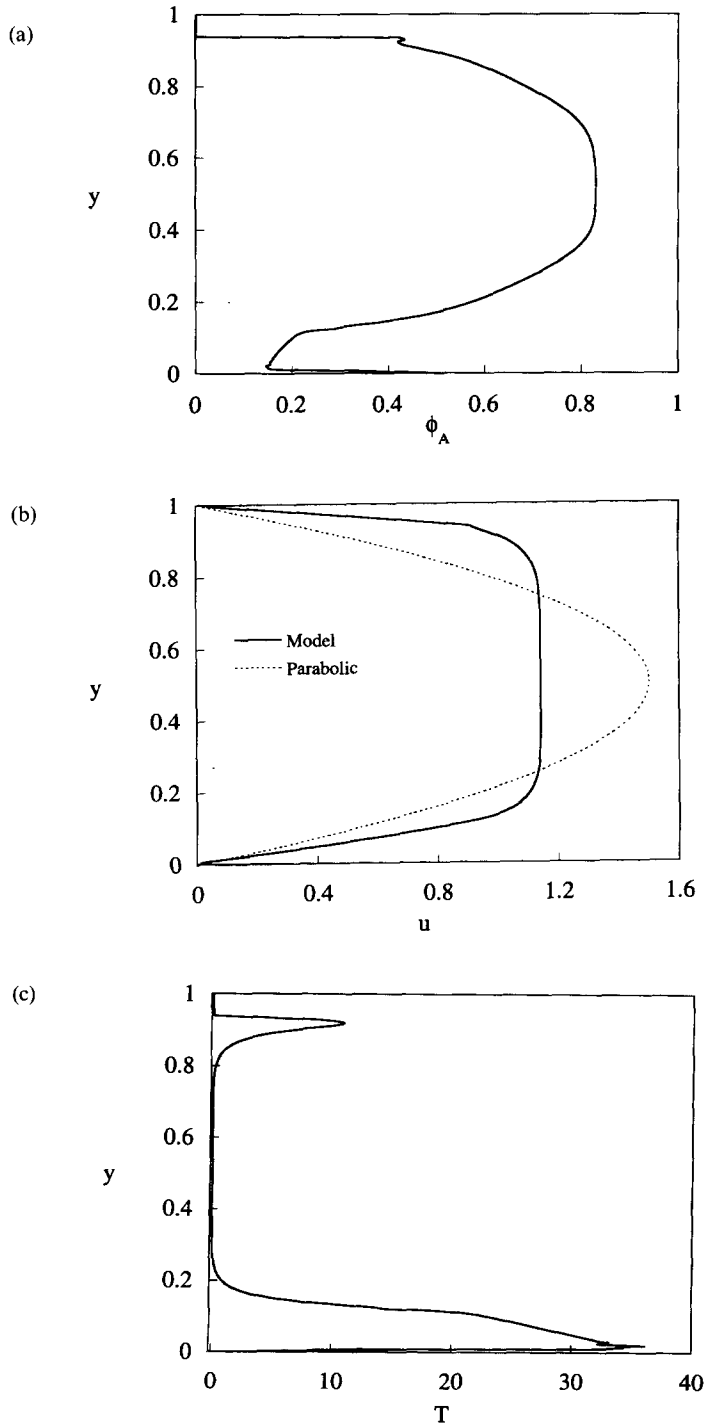

Figure 9. Model predictions for the fully-developed flow of a suspension at $\phi_A^b = 0.6$, $B = 5$, and $H/a = 100$: (a) particle fraction ϕ_A (b) the suspension velocity u, and (c) suspension temperature T. The parabolic velocity profile of a Newtonian fluid at the same volumetric flux is shown in (b).

5. SUMMARY AND CONCLUDING REMARKS

Channel flow of a suspension of dense particles flowing in a monolayer was simulated by Stokesian Dynamics over a range of the bulk particle area fraction ϕ_A^b, dimensionless channel width H/a, and buoyancy parameter $B = (U^0/\langle u \rangle)(H/a)^2$. The simulations provide basic information which is unavailable from present experimental results. Direct comparisons between simulation results and predictions of the flow by the suspension balance model have established the validity of the model under conditions where buoyancy is relevant. Buoyancy effects can be continuously varied, and a large range of behavior is exhibited. For intermediate to large values of B, the fully-developed flow is quite unlike that of a neutrally-buoyant suspension in pressure-driven flow. Good agreement between simulation and model predictions with flow behavior over a range of B and ϕ_A^b, with model parameters fitted at a single condition, indicates that the constitutive modeling proposed is capable of explaining the observed behavior.

Pressure-driven flow of a suspension of dense particles results in the somewhat surprising phenomenon of a relatively heavy material flowing over light, first shown by Altobelli *et al.* (1991). Zhang and Acrivos (1994) have used the diffusive-flux phenomenology of Leighton and Acrivos (1987b) to predict this flow, finding good agreement with the experiments of Altobelli *et al.* for the fully-developed flow, including the noted stratification. They also find that the model predicts a mean secondary non-axial flow; it does not, however, appear that the diffusive-flux model could predict the density stratification seen in the channel flow simulations. A study of the diffusive-flux model for the flow shows it would require a cross-stream flux proportional to $\nabla \dot\gamma$ to balance the gravity-driven flux where $\dot\gamma = 0$; the mechanism which drives a flux toward the velocity maximum would now have to drive particles away from this point. While resuspension in tube flow is more complicated than in channel flow, owing to the secondary flow produced by the density stratification, channel flow actually provides the more stringent test of basic aspects of the flow model. Because the cross-stream particle flux balance in the fully-developed channel flow is one-dimensional, the excess weight of the dense suspension at the center of the channel must be supported by a stress variation directly related to the shear-induced migration. Thus the manner in which migration is incorporated into the model is isolated for scrutiny.

The aphysical predictions (Phillips *et al.* 1992) of the diffusive-flux model result from its locality in $\dot\gamma$. The suspension-balance model as employed in the present work achieves a nonlocality in $\dot\gamma$ indirectly by assuming the particle pressure to depend on the suspension temperature as $\sqrt{T}$. An equation for T, whose form is deduced by physical arguments from the balance equation governing the microscopic kinetic energy in the suspension, includes diffusion of T, so that fluctuational motion is produced in regions of large $\dot\gamma$, with diffusive transport to regions of small or zero $\dot\gamma$.

Simulations show that the flow behavior depends strongly upon both ϕ_A^b and B, but only weakly upon H/a. The weakness of the dependence on H/a is largely due to the fact that the influence of particle size has been included in B; consistent with the finding of NB for $B = 0$, the primary influence of H/a at nonzero B is upon the suspension temperature, as T is larger in the weakly-sheared regions for smaller H/a and varies rapidly near the walls in a layer whose thickness scales roughly as a/H. At fixed ϕ_A^b and H/a, increasing B has the expected effect of driving particles toward the lower wall, but the maximum ϕ_A often lies above the channel centerline. As a result, there is heavy suspension over light, and this occurs for a wide range of B for moderate concentrations. The strong dependence of the flow behavior on ϕ_A^b reflects the strong dependence of the viscosity upon particle fraction.

Confidence in suspension-flow modeling in which T is a variable of central importance is increased by the success of the suspension-balance model in this study. We have tested the model over a range of conditions, and it should be noted also that a new type of nonlinearity in T is introduced by particle buoyancy (see [33]). The equation for T, unlike the others in the model, was deduced rather than derived, and its boundary conditions caused some difficulties in the original application. The success with which the model predicted the T field, including some unexpected behavior, indicates that the physical arguments used in deducing the equation are sound. The *ad hoc* boundary condition applied to T is also successful and, although unsatisfying because it retains considerable freedom in its specification, accurately reflects the hydrodynamic damping effect of

a solid boundary. With the work of NB and the present investigation establishing the validity of this model in a straight channel, it would be of interest to know its predictions for other geometries, including rheometric flows and flows in curved channels or pipes.

In closing, we emphasize that the use of T is a modeling assumption to deal with the problems encountered when $\dot{\gamma} = 0$. The essential merit of the suspension balance approach is that it shows the direct coupling of the particle-phase mass and momentum equations, demonstrating how the particle flux is related to the variation of the bulk stress. This approach shows that for particle migration to occur the suspension must be non-Newtonian, because it is a normal stress variation, and not a shear stress variation, which drives the cross-stream particle flux. In the work of NB, it was shown that the diffusive-flux approach as essentially contained in the suspension-balance model, and Zhang and Acrivos (1994) assert that the two models are very similar. Indeed, the microstructural arguments involving irreversible interparticle interactions put forward by Leighton and Acrivos (1987b) to generate particle migration are precisely those necessary to generate normal stresses as shown by Brady and Morris (1997). However, in its rheological basis, which recognizes that suspensions exhibit shear-induced normal stresses and in showing that the particle flux results from the influence of these stresses, the suspension-balance approach has fundamental differences from the diffusive-flux modeling.

REFERENCES

Altobelli, S. A., Givler, R. C. and Fukushima, E. (1991) Velocity and concentration measurements of suspensions by nuclear-magnetic-resonance imaging. *J. Rheol.* **35**, 721–734.

Batchelor, G. K. (1970) The stress system in a suspension of force-free particles. *J. Fluid Mech.* **41**, 545–570.

Beenakker, C. W. J. (1986) Ewald sum of the Rotne–Prager tensor. *J. Chem. Phys.* **85**, 1581–1582.

Bender, C. M. and Orszag, S. A. (1978) *Advanced Mathematical Methods for Scientists and Engineers*. McGraw-Hill, New York.

Bender, J. W. and Wagner, N. J. (1996) Reversible shear thickening in monodisperse and bidisperse colloidal dispersions. *J. Rheol.* **40**, 899–916.

Bossis, G. and Brady, J. F. (1989) The rheology of Brownian suspensions. *J. Chem. Phys.* **91**, 1866–1874.

Brady, J. F. (1993) The rheological behavior of concentrated colloidal dispersions. *J. Chem. Phys.* **99**, 567–581.

Brady, J. F. and Bossis, G. (1988) Stokesian Dynamics. *Ann. Rev. Fluid Mech.* **20**, 111–157.

Brady, J. F. and Morris, J. F. (1997) Microstructure of strongly-sheared suspensions and its impact on rheology and diffusion. *J. Fluid Mech.*, in press.

Brady, J. F., Phillips, R. J., Lester, J. C. and Bossis, G. (1988) Dynamic simulation of hydrodynamically interacting suspensions. *J. Fluid Mech.* **195**, 257–280.

Davis, R. H. and Acrivos, A. (1985) Sedimentation of noncolloidal particles at low Reynolds numbers. *Ann Rev. Fluid Mech.* **17**, 91–118.

D'Haene, P., Mewis, J. and Fuller, G. G. (1993) Scattering dichroism measurements of flow-induced structure of a shear thickening suspension. *J. Colloid Interface Sci.* **156**, 350–358.

Durlofsky, L. and Brady, J. F. (1989) Dynamic simulation of bounded suspensions of hydrodynamically interacting spheres. *J. Fluid Mech.* **200**, 39–67.

Eckstein, E. C., Bailey, D. G. and Shapiro, A. H. (1977) Self-diffusion in shear flow of a suspension. *J. Fluid Mech.* **79**, 191–208.

Gadala-Maria, F. (1979) The rheology of concentrated suspensions. Ph.D. Thesis, Stanford University.

Gadala-Maria, F. and Acrivos, A. (1980) Shear-induced structure in a concentrated suspension of solid spheres. *J. Rheol.* **24**(6), 799–814.

Irving, J. H. and Kirkwood, J. G. (1950) The statistical mechanical theory of transport processes IV. The equations of hydrodynamics. *J. Chem. Phys.* **18,** 817–829.

Jeffrey, D. J., Morris, J. F. and Brady, J. F. (1993) The pressure moments for two spheres in a low-Reynolds-number flow. *Phys. Fluids A* **5,** 2317–2325.

Jenkins, J. T. and McTigue, D. F. (1990) Transport processes in concentrated suspensions: the role of particle fluctuations. In *Two Phase Flows and Waves*, eds D. D. Joseph and D. G. Schaeffer. Springer, Berlin.

Kausch, H. H., Fesko, D. G. and Tschoegl, N. W. (1971) The random packing of circles in a plane. *J. Colloid Interface Sci.* **37,** 603–611.

Kim, S. and Karrila, S. J. (1991) *Microhydrodynamics: Principles and Selected Applications.* Butterworth-Heinemann, London.

Koh, C. J., Hookham, P. and Leal, L. G. (1994) An experimental investigation of concentrated suspension flows in a rectangular channel. *J. Fluid Mech.* **266,** 1–32.

Krieger, I. M. (1972) Rheology of monodisperse lattices. *Adv. Colloid Interface Sci.* **2,** 111–136.

Leighton, D. and Acrivos, A. (1986) Viscous resuspension. *Chem. Eng. Sci.* **41,** 1377–1384.

Leighton, D. and Acrivos, A. (1987a) Measurement of self-diffusion in concentrated suspensions of spheres. *J. Fluid Mech.* **177,** 109–131.

Leighton, D. and Acrivos, A. (1987b) The shear-induced migration of particles in concentrated suspensions. *J. Fluid Mech.* **181,** 415–439.

Mills, P. and Snabre, P. (1996) Rheology and structure of concentrated suspensions of hard spheres. Shear induced particle migration. *J. de Phys. II* **5,** 1597–1608.

Nott, P. R. and Brady, J. F. (1994) Pressure-driven suspension flow: Simulation and theory. *J. Fluid Mech.* **275,** 157–199.

Parsi, F. and Gadala-Maria, F. (1987) Fore-and-aft asymmetry in a concentrated suspension of solid spheres. *J. Rheol.* **31,** 725–732.

Phillips, R. J., Armstrong, R. C., Brown, R. A., Graham, A. and Abbott, J. R. (1992) A constitutive model for concentrated suspensions that accounts for shear-induced particle migration. *Phys. Fluids A* **4,** 30–40.

Phillips, R. J., Brady, J. F. and Bossis, G. (1988) Hydrodynamic transport properties of hard-sphere dispersions. I. Suspensions of freely mobile particles. *Phys. Fluids* **31,** 3462–3472.

Phung, T. N. (1993) Behavior of concentrated colloidal dispersions by Stokesian Dynamics. Ph.D. Thesis, California Institute of Technology.

Phung, T. N., Brady, J. F. and Bossis, G. (1996) Stokesian Dynamics simulation of Brownian suspensions. *J. Fluid Mech.* **313,** 181–207.

Schaflinger, U., Acrivos, A. and Zhang, K. (1990) Viscous resuspension of a sediment within a laminar and stratified flow. *Int. J. Multiphase Flow* **16,** 567–578.

van der Werff, J. C. and de Kruif, C. G. (1989) Hard-sphere colloidal dispersions: the scaling of rheological properties with particle size, volume fraction, and shear rate. *J. Rheol.* **33,** 421–454.

Zhang, K. and Acrivos, A. (1994) Viscous resuspension in fully developed laminar pipe flows. *Int. J. Multiphase Flow* **20,** 579–591.